THIN-SUSPENDED 2D HETEROSTRUCTURES: DETERMINISTIC TRANSFER AND TUNABLE GRAPHENE LIGHT ABSORPTION

ISRAEL GOMEZ REBOLLO

A THESIS

IN

THE DEPARTMENT

OF

PHYSICS

PRESENTED IN PARTIAL FULFILLMENT OF THE REQUIREMENTS
FOR THE DEGREE OF MASTER OF SCIENCE
CONCORDIA UNIVERSITY
MONTRÉAL, QUÉBEC, CANADA

SEPTEMBER 2020

Concordia University
School of Graduate Studies

This is to certify that the thesis prepared

By: **Israel Gomez Rebollo**

Entitled: **Thin-Suspended 2D Heterostructures: Deterministic Transfer and Tunable Graphene Light Absorption**

and submitted in partial fulfillment of the requirements for the degree of

Master of Science

complies with the regulations of this University and meets the accepted standards with respect to originality and quality.

Signed by the final examining commitee:

Valter Zazubovits	Chair
Pablo Bianucci	Examiner
Ingo Salzmann	Examiner
Alexandre Champagne	Supervisor

Approved ___Valter Zazubovits_____

Chair of Department or Graduate Program Director

_____ 20 _____ ___Pascale Sicotte_____

Dean of Faculty

Abstract

Thin-Suspended 2D Heterostructures: Deterministic Transfer and
Tunable Graphene Light Absorption

Israel Gomez Rebollo

We report a deterministic 2D material (2DM) transfer method to assemble any-stacking-order heterostructures incorporating suspended ultra-thin 2D materials, such as single (SLG) and bilayer graphene (BLG). This high-yield and facile transfer method will enable fabrication of 2DM heterostructures suited for nano-opto-electro-mechanical (NOEMS) studies, such as optical transducers where a small gate voltage moves a suspended 2DM to vastly enhance or suppress its exclusive light absorption. Our transfer procedure is based on a 3 dimensional (3D) nitrocellulose micro-stamp which can dry pick-up single and naked 2DMs (graphene, MoS_2, and hBN) directly from a SiO_2 substrate, and deterministically transfer them on substrates or suspend them over trenches. Optical and Raman spectroscopy show that no significant defects and doping is introduced upon transfer, even in suspended SLG and BLG. The transferred area of ultra-thin 2D crystals ranges up to 600 μm^2. The suspension procedure does not require critical point drying, and transfers ultra-thin 2DM areas up to 15 μm^2 with suspension heights down to 550 nm. Using this fabrication method, we assembled optical cavities able to accurately tune the Raman scattering intensity and exclusive light absorption on both on substrate and suspended BLG by factors of 19 and 4 respectively. This deterministic fabrication of heterostructures incorporating suspended 2DMs is likely to accelerate research in twistronics, straintronics and NOEMS.

Acknowledgments

The completion of this project would not have been possible without the great help of my supervisor Alexandre Champagne, project college Fernanda Rodrigues and my lab peers Gareth, Andrew, Matthew, Guoqing, Linxiang and Wyatt. Fernanda helped so much in developing the transfer method, thanks to her creativity we were able to make a state-of-the-art stamping setup capable of directly suspending ultra-thin 2D materials. Matthew and Andrew taught me about micro-fabrication, Gareth showed me how to take and analyse Raman spectroscopy measurements, and the others helped me all along the project.

A special thanks to my partner Roxane, she had to put up with my all night working sessions and bad mood at times. Without her support and love I don't know how I could have done it.

Physics is so powerful and sometimes frightening hard. I had to work really hard to grasp many of the most important concepts, however, I feel empowered at the end of this road. This part of my life has been one of the most rewarding and challenging so far.

Contents

List of Figures

List of Tables

List of Equations

Chapter 1

Introduction: Fabrication of Suspended 2-Dimensional Systems

Major advances in the ability to mechanically transfer, align, and stack 2D materials (2DMs)[1, 2] to form pristine heterostructures [3, 4], have greatly accelerated experiments in quantum electron transport [5, 6, 7] and optoelectronics [8, 9], over the last several years. The wide array of transfer methods now available can assemble most of the viable vertically-stacked 2D heterostructures, with one major set of exceptions. There is no flexible (any 2DM, any stacking order) and deterministic (with alignment) procedure to assemble 2D heterostructures which incorporates layers of vacuum/air, i.e., suspended, ultra-thin 2DMs. Indeed, previous transfer methods for heterostructures incorporating suspended 2DMs have either used thick-suspended 2D crystals [10, 11], non-deterministic transfer of thin-suspended 2DMs [5], or developed single-purpose custom micro/nanofabrication routes for each device geometry [4]. The research needs for incorporating suspended 2DMs in precisely assembled heterostructures are many. Such devices would permit unprecedented levels of simultaneous control of electronics, mechanics, optics and their interactions in Nano-opto-electro-mechanical systems (NOEMS) [11, 12]. For example, vacuum layers offer a uniquely different index of refraction to optimize exciton binding energy and lifetime in 2DMs [13]. In quantum transport studies of twisted bilayer 2DMs (twistronics)[14], properly designed suspension would permit one to decouple the mechanically sensitive bilayers from the substrate's strain to strain-engineer [15, 16], their quantum phases [17, 18]. Last but not least, stacking 2D NEMS atop 2D

1

heterostructures to create optical cavities [19, 20, 21], can enhance light-matter interactions enough to hybridize photonics with NEMS physics [13, 22, 23, 5, 24].

In this thesis we present the development of a 2D material assembly method able to dry pick-up ultra-thin naked (i.e., not encapsulated) 2DM directly from SiO_2 and transfer them on substrates or trenches using only microliter amounts of mild solvents (see Figure 1.1). To do so, we use a facile and rapid stamping procedure which relies on a nitrocellulose micro-stamp (~ 200 μm wide) deposited on a glass slide and a standard micromanipulator stamping instrumentation. It permits the rapid transfer of thin 2DMs (graphene, MoS_2, and hBN) with areas up to 600 μm^2 without introducing defects, to different substrates (SiO_2, hBN, Aluminum) with a single robust recipe and to align various crystals. The transferred crystals are not damaged, confirmed via optical and Raman spectroscopy, and can be picked-up and deposited deterministically with two-μm precision. We demonstrate the assembly of high-quality 2D hetorostructures, both on substrate, bilayer-graphene/hBN/Al, and suspended above exfoliated hBN trenches, single and bilayer-graphene/air/SiO_2, without any clean-room instrumentation. The suspension procedure does not require critical point drying, and transfers ultra-thin 2DM with areas up to 15 μm^2 and with suspension heights down to 520 nm. An application of this transfer assembly is demonstrated by engineering the exclusive light absorption of both on-substrate and suspended SLG and BLG fabricated optical cavities. Given the exceptional electronic and mechanical properties of BLG, maximizing its light absorption would improve the prospects of light harvesting and photo-electric devices [9, 19, 21, 25]. We demonstrate a quantitative agreement between first principle theory of Raman intensity, and the underlying exclusive light absorption, and the experimental Raman spectra on several BLG/hBN/Al and BLG/Air/SiO_2 cavities. We find that the BLG Raman scattering factor and light absorption can be tuned by factors of 19 and 3.8 respectively in the supported and suspended heterostructures. We continue this chapter with brief view of the recent developments in 2D transfer fabrication with a focus on suspended devices. We also review the necessary graphene optical properties to understand the first-principles models used in chapter 3. Graphene light absorption and Raman light scattering.
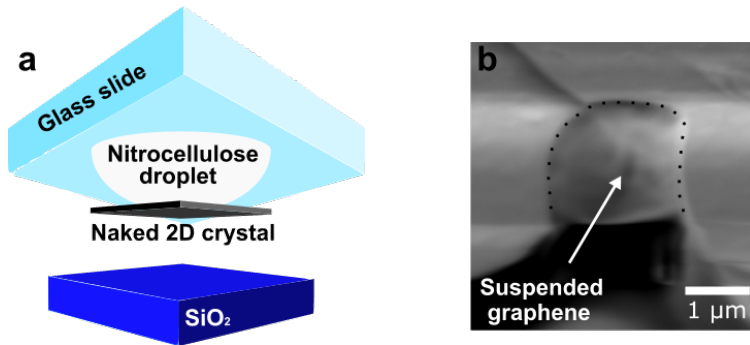
Figure 1.1: Stamping naked and suspended 2D materials. (a) Schematic diagram of our nitrocellulose-based stamping method. (bottom) SiO_2/Si substrate. (middle) A naked 2D crystal adhered to the nitrocellulose micro-stamp. (top) The nitrocellulose micro-stamp facing downwards held onto a glass slid. (b) Tilted scanning electron micrograph of suspended BLG on a hexagonal boron nitride trench, suspended area of approximately 4 μm^2 (black dots as guide to the eye)

1.1 Transfer of 2DMs into heterostructures

Fabrication of 2DM heterostructures is achieved by epitaxial growth, a process which relies on strong chemical bonds and material compatibility. Van der Walls (vdW) integration of 2DMs into heterostructures has no such limitations [4] and this stamping method have proven to have great stability [26]. The stacking of different 2DMs together can induce structural changes in each other [3] and understanding these interactions is critical for their manipulation [28]. For instance, it has been reported that graphite experiences stronger vdW interactions with MoS_2 than with hBN [5]. Our transfer method allows to transfer exfoliated, single and naked 2DMs directly from a SiO_2/Si substrate in as little as one hour. Existing methods use intermediary 2DMs, such as hBN [27, 29, 31, 30, 32] or tungsten diselenide (WSe_2) flake [33] to accomplish the direct pick-up, but end up encapsulating the graphene crystal. Others use the capillary forces of water-based solution on polydimethylsiloxane (PDMS) to transfer graphene (Gr) and molybdenum disulfide (MoS_2) naked crystals [34]. Our simple, fast and reliable stamping method works for graphene , hBN and MoS_2. We made 20 on susbstrate devices with a high success rate of 95%. Most importantly, we can use our fabrication technique to directly suspend large-area single layer (SLG) and bilayer (BLG) graphene without the use of any clean room equipment, such as lithography, chemical/physical etching or critical point drying (CPD).
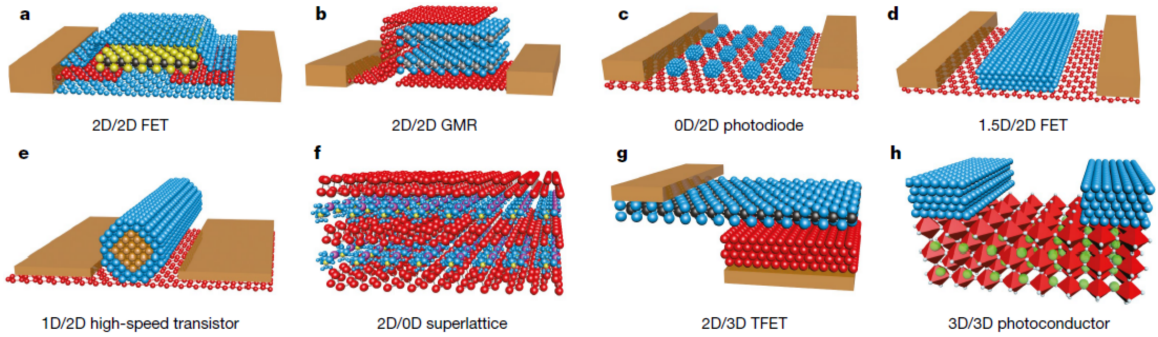
Figure 1.2: Diagram of state-of-the-art vdW-integrated electronic and optoelectronic devices. (a) 2D/2D encapsulated planar transistor. (b) 2D/2D vdW magnetic vertical tunnelling junction. (c) 0D/2D photodiode with vdW integration of quantum dots (blue) on top of graphene (red). (d) 1.5D/2D top-gate FET. (e) 1D/2D highspeed transistor made of nanowire on top of graphene (red). (f) 2D/0D high-order superlattice made of quantum dots intercalated with 2D semiconductor. (g) 2D/3D high-efficiency electron tunnelling transistor. (h) 3D/3D vdW integration of metal contacts to avoid metallization. Figure reproduced from [4].

1.1.1 Why naked and suspended 2DMs?

The goal of fabricating pristine and suspended individual 2DMs is to be able to gain access to the mechanical properties [35]. Systems that couple optical, electrical and mechanical properties of 2DMs are under development in many laboratories around the globe. Such systems allow the control of opto-electronic properties by mechanical deformations of suspended 2DMs [12, 36, 24]. Most widely-used methods to suspend 2DMs use a sacrificial layer, such as a lift-off-resist (LOR) [37, 38] or silicon dioxide (SiO_2) [24, 39]. The 2DM is then clamped by the patterning of metal contacts and the sacrificial layer is etched "away" followed by a CPD to avoid collapse. Other, more complex methods for suspending 2DMs start with the growth of a water-soluble $Sr_3Al_2O_6$ sacrificial layer, the 2DM is grown or stamped on top of this layer, and finally the sacrificial layer is dissolved to suspend the 2D crystal above a patterned substrate [40]. Such stamping methods for suspending 2DMs required several, sometimes complex, steps and have major limitations on the dimensions of the suspended crystal area and relatively low yields. Our fabrication method is capable of manipulating single and pristine 2D crystals to directly suspend them over trenches, with suspension height as low as 550 nm for one-atom-thick crystals. We made 14 suspended graphene devices; our success rate was 93%. We used atomic force microscopy (AFM) and tilted scanning electron microscopy (SEM) to characterize our

suspended structures. In Figure 1.3a, NOEMS combine electronics, mechanics and optics. In Figure 1.3b, we show a proposal we conceived based on our 2D transfer approach, where a 2DM can be mechanically deflected by electrostatic force, allowing to enhance/suppress the light absorption in the active 2DM. This is possible due to constructive and destructive light interferences as the thickness of the optical cavity is modulated.
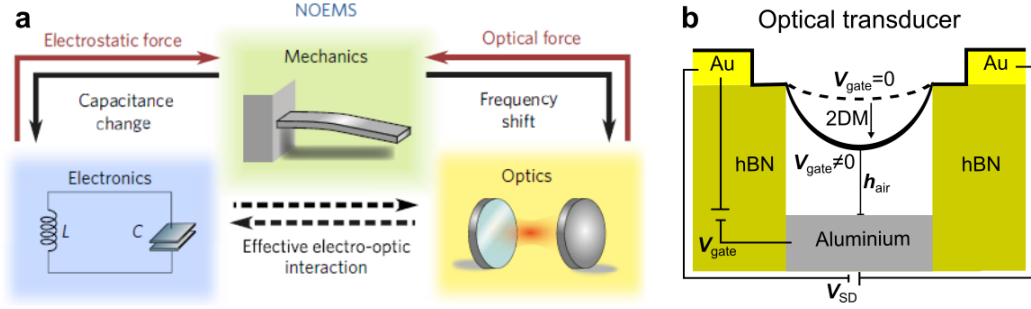
Figure 1.3: Nano-opto-electromechanical systems. (a) NOEMS combine electronics, mechanics, and optics. Reproduced from [12]. (b) Schematic diagram of an optical transducer made of suspended BLG stamped on an hBN trench with Au contacts and an aluminium reflector at the bottom of the trench. A small gate voltage is applied to deflect the BLG, this will tune its light absorption by interference effects. Photocurrent measurements can be done due to source-drain Au contacts.

1.2   Graphene light absorption

Graphene is known for its electronic as well as for its optical and mechanical properties. Its optical properties and electronic properties are due to its peculiar band structure that is described in terms of Dirac fermions at the edge of the Brillouin zone [41, 42]. Graphene is made out of carbon atoms arranged in a hexagonal lattice; it has a basis of two atoms per unit cell at a distance of $a = 1.42 \mathring{A}$. In the first Brillouin zone (k-space) there are two important points K and K', called Dirac points (see Figure 1.4). With this information and the use of the tight-binding model, the electronic states of monolayer graphene can be obtained. The electronic dispersion relation near these points has a linear relationship of the form [41],

$$\hat{H}(\vec{k}) = \hbar v_{\mathrm{F}} \vec{\sigma} \cdot \vec{k} \tag{1.1}$$

5
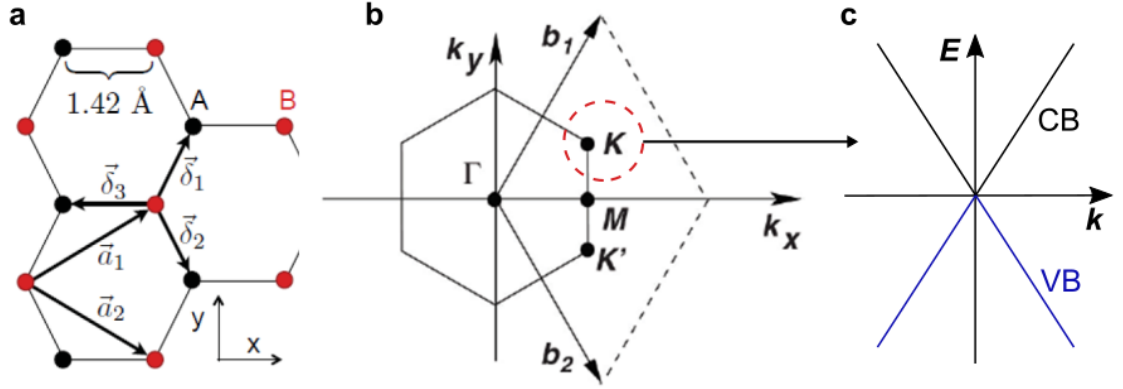
Figure 1.4: Graphene lattice and dispersion relation. (a) Graphene lattice structure. (b) Dirac points in first Brillouin zone. (c) Electronic dispersion relation at the K point.

The absorption of electromagnetic radiation in graphene is controlled by interband and intraband transitions [43] (see Figure 1.5). When light interacts with graphene it can be reflected (R), absorbed (A) or transmitted (T). By appying energy conservation we get the relationship $R + A + T = 1$. Theoretical models predict an almost negligible reflection from graphene $R_{\mathrm{SLG}} \approx 0.1\%$, an absorption of $A_{\mathrm{SLG}} \approx 2.3\%$ and transmission of $T_{\mathrm{SLG}} \approx 97.6\%$, which has been experimentally measured [44, 45]. The Beer-Lambert law states the relationship between incident light intensity and light intensity at a later stage. It relates the attenuation of light to the optical properties of the material through which it is travelling. The light intensity as a function of position z (for x and y remaining constant) is,

$$I(z) = I_0 e^{-\alpha_{\mathrm{abs}}(\omega)z} \tag{1.2}$$

Where the term $\alpha_{\mathrm{abs}}(\omega)$ is the absorption coefficient that depends on the photon's frequency ω (energy), and I_0 is the incident intensity. The light intensity exponentially decays as a function of both the absorption coefficient and the z position. This coefficient is related to the complex index of refraction $\tilde{n}$ of the material in which the light is transmitted,

$$\tilde{n} = n(\omega) + i\kappa(\omega) \tag{1.3}$$

Where $n(\omega)$ and $\kappa(\omega)$ are the real and imaginary parts. The absorption coefficient can be expressed as,

$$\alpha_{\text{abs}}(\omega) = \frac{2\omega\kappa(\omega)}{c_0} \tag{1.4}$$

Where c_0 is the light speed in vacuum. We only need to know the imaginary part of the complex index of refraction for a particular photon energy to compute the transmitted light intensity and is related to the dielectric constant $\varepsilon(\omega)$. The square of the complex index of refraction is [46],

$$\tilde{n}^2(\omega) = \varepsilon(\omega) = 1 + \frac{4\pi i\sigma(\omega)}{\omega} \tag{1.5}$$

Where $\sigma(\omega)$ is the conductivity of the material. For solids we have to sum the contributions from intraband and interband processes. Intraband processes refer to the electronic conduction by free carriers in conducting materials like metals and depend on the photon's energy. These give rise to the complex Drude conductivity σ_D, according to classical Drude theory. Interband processes are when an electron (below the Fermi level) in the valence band is photo-excited to the conduction band and are described in terms of quantum mechanics (see Figure 1.5). In the case of graphene there is no band gap because the valence and conduction bands touch at the Dirac point (K, K' points). The transition rate is determined by Fermi's Golden Rule between the π (valence band) and π^* (conduction band) states [46]. We get a value for the interband conductivity of $\sigma_i = e^2/4\hbar$, which is a quantum of conductance and has no dependence on the photon's energy [45]. The dielectric constant expressed in terms of these two conductivity contributions σ_D and σ_i is,

$$\varepsilon(\omega) = 1 + \frac{4\pi i}{\omega}[\sigma_D(\omega) + \sigma_i] \tag{1.6}$$

We can simplify this expression by dropping the Drude term as the interband

7

processes dominate in the visible range of light.

$$\tilde{n}(\omega) = \sqrt{1 + \frac{4\pi i}{\omega}\sigma_i} \tag{1.7}$$
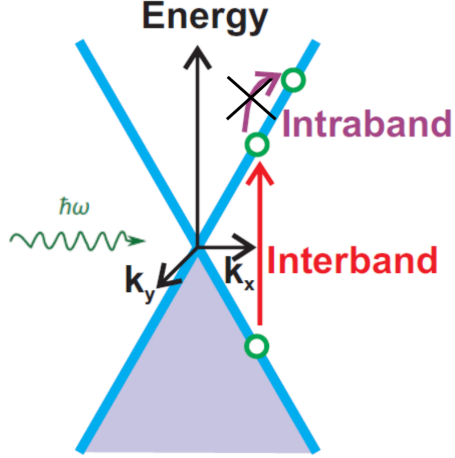
Figure 1.5: (a) Schematic band structure of undoped ($\mu_F = 0$) graphene near the Dirac point demonstrating the interband and intraband dynamics. Only interband contributions are possible in the visible range of light, figure modified from [43].

We clearly see that $\sigma_i << \omega$ and by a series expansion of the square root, we simply get the imaginary part κ of the index of refraction n. Now our coefficient of absorption is,

$$\alpha_{\mathrm{abs}}(\omega) = \frac{2\omega\kappa}{c_0} \approx \frac{4\pi\sigma_i}{c_0} \approx \frac{\pi e^2}{\hbar c_0} \approx \pi\alpha \tag{1.8}$$

Where $\alpha = e^2/\hbar c$ is the fine structure constant. Now we can compute the light absorption by a single layer of graphene,

$$A_{\mathrm{SLG}} = 1 - T_{\mathrm{SLG}} - R_{\mathrm{SLG}} \approx 1 - e^{-\pi\alpha} \approx \pi\alpha \approx 2.3\% \tag{1.9}$$

The fine structure constant α is the parameter that describes the coupling between light and relativistic electrons; it is normally associated with quantum electrodynamics rather than condensed matter physics. In Figure 1.6, the experimental light transmittance of graphene is detailed. In Figure 1.6a, we can

see the optical image of a graphene crystal suspended on a metal ring placed under vacuum. This crystal consists of monolayer and bilayer covering two thirds of the ring (right side). A xenon lamp with wavelength λ_{laser} between 400 and 800 nm was used as a light source. In Figure 1.6b, the plot of light transmittance as a function of wavelength is shown. The light transmission over this range does not change considerably, as expected from theory. For more than one layer of graphene, the absorption is linear up to few layers [45]. Given the one-atom-thickness of SLG, it has strong light absorption, and the lack of a bandgap means no light emission is possible. However, light scattering occurs in graphene in the form of inelastic Raman scattering [47, 48].
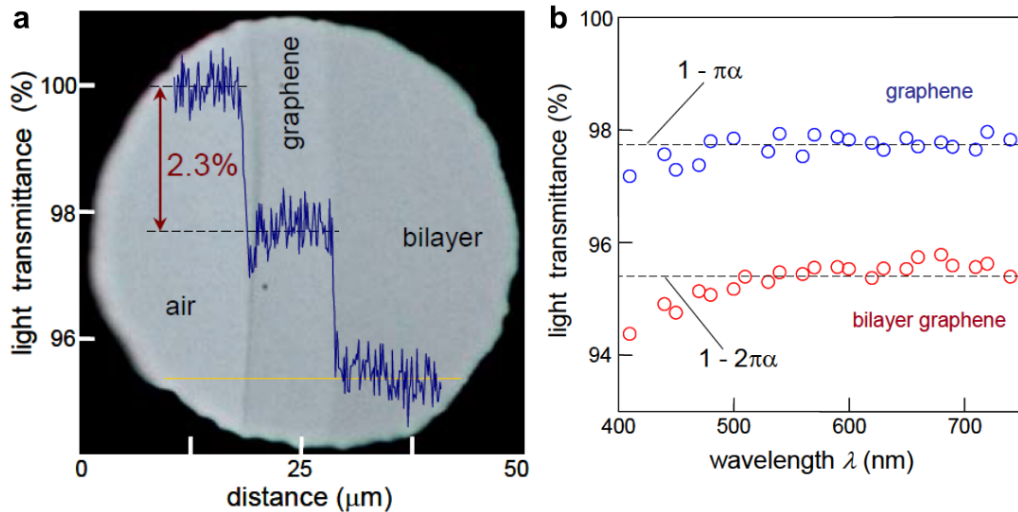
Figure 1.6: Light transmittance in SLG and BLG. (a) Optical photograph of a metal ring partially covered by SLG and BLG. The line scan profile shows the intensity of transmitted white light along the yellow line. (b) Transmittance spectra of single and bilayer regions of the sample shown in (a). Figure reproduced from [45].

1.3   Graphene Raman light scattering

Raman light scattering in graphene occurs when an incident photon is absorbed by an electron-hole pair, then a single phonon (G band) or a combination of phonons (2D band) is emitted. The electron then recombines with the hole with the emission of a photon of lower energy than the incident one (see Figure 1.7). By conservation of energy, the scattered photon and phonon energies add up to the incident photon's

energy [49, 50]. The photon energy difference is measured to learn about the energy of the phonon modes and their dynamics [51]. The electronic structure of graphene is uniquely captured in its Raman spectrum [47, 52, 53]. It is used to determine the number and orientation of layers, the quality and types of edge, and the effects of perturbations, such as electric and magnetic fields, strain, doping, disorder and, importantly for our purposes, the defect density [48, 57, 55]. We use the Raman spectrum to easily distinguish the different materials involved in our optical cavities and to indirectly measure the graphene exclusive light absorption.
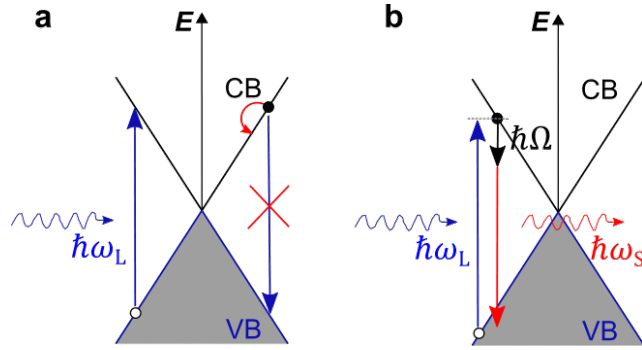
Figure 1.7: Graphene light absorption, emission and scattering. (a) An incident photon with frequency ω_L excites an electron from the valence to the conduction band. No photon emission occurs in graphene due to the lack of a band gap, the excited electron thermally relaxes to then recombine with the hole. (b) The photo-excited electron produces a phonon with frequency Ω in its transition to the conduction band. The electron and hole then recombine to emit a Raman scattered photon with frequency ω_S.

As we can see in Figure 1.8 the Raman spectrum of pristine monolayer graphene features two prominent peaks. One is associated with the longitudinal optical phonon (LO) mode, occurring around 1580 cm^{-1} and is called the G peak, and the other is an especially intense second order Raman feature called the 2D peak at around 2700 cm^{-1} [49, 56]. The first order G peak involves a zone-center optical phonon at the Γ point and the second order 2D peak involves near zone-edge optical phonons at the K and K' points (see 1st Brillouin zone in Figure 1.4b). There is a third peak called the D peak (around 1340 cm^{-1}) and is related to the presence of defects in the lattice, such as missing carbon atoms or the introduction of other type of atoms [55].

10
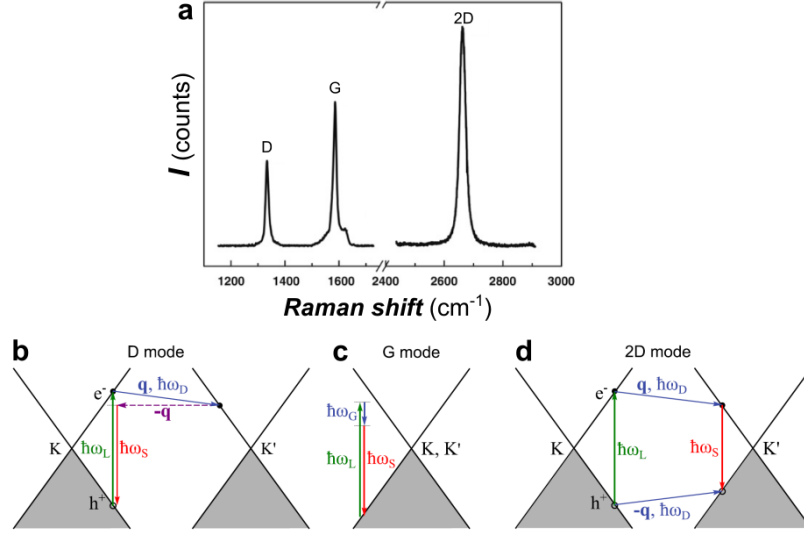
Figure 1.8: Raman spectrum of SLG. (a) Raman spectrum featuring three prominent peaks, the defect-induced D, the first order G and higher order 2D peaks. (b)-(d) Schematics of the tree Raman peaks. $\hbar\omega_L$ ($\hbar\omega_S$) denote the incoming laser (Raman scattered) photon energy. (b) The D peak involves one electron-phonon (solid arrow) scattering (q, ω_D) and one electron-defect (dashed arrow) scattering process. (c) The G peak is a non-resonant process. (d) The 2D peak involves two phonons with frequency ω_D and opposite momentum $\pm q$. Figure reproduced from [55].

1.4 Thesis structure

The original research work contained in this thesis is presented in Chapters 2 & 3. In Chapter 2, we describe in detail our novel transfer process built upon the use of a highly transparent and soluble micro-stamp made of nitrocellulose polymer. Its fabrication capabilities, and how it differs from other widely-used state-of-the-art transfer methods found in literature. We show the fabrication of several on-substrate and suspended heterostructures made with graphene, hBN, and MoS_2 of different dimensions, thickness and geometry. These structures are then characterized using Raman spectroscopy to demonstrate that no significant defect or doping is introduced upon transfer, even in ultra-thin 2DM devices. AFM and tilted SEM are used to directly measure our heterostructures dimensions. We finally summarize in two tables all 34 fabricated devices, 20 on susbtrate and 14 suspended. We had a fabrication success rate of 95% and 93%, respectively.

In Chapter 3, we make use of two simple experimental models based on first-principles to calculate the exclusive light absorption (A_{Gr}) and Raman signal

enhancement factor (F_{Gr}) of graphene. We wrote a couple pieces of Mathematica code to implement the models, make predictions and guide our device fabrication. We detail the experimental results of micro-Raman measurements on various graphene-based optical cavities; the calibration of our measurements makes sure it is reproducible and reliable. We show the connection of both models to extract the exclusive light absorption from Raman intensity data, this works for both wavelengths (G and 2D peaks) present in our measurements. We present four stamped optical cavities made of BLG/hBN/Aluminium with varying hBN-spacer thickness, in which we accomplished an on/off ratio of 19 for the Raman factor that translates into an on/off ratio of 18 for the exclusive light absorption. We also present one tilted optical cavity made of BLG/Air/SiO$_2$, where we were able to tune the Raman factor by 3.8 and the exclusive absorption by 6.3. Finally, two suspended BLG and one suspended SLG with different suspension heights are also measured and modelled, as these are the basis for the near future continuation of this project.

In chapter 4, we summarize the three major results of this thesis: the all-dry pick-up of 2DMs directly from SiO$_2$ and their subsequent suspension over hBN trenches by our transfer method, as well as the ability to tune the Raman scattering and exclusive light absorption of graphene in several devices. We present applications of nano-opto-electro-mechanical systems and a discussion on the near future of this project. We show the ongoing fabrication of an optical transducer where a small gate voltage moves a suspended BLG to vastly enhance/suppress its exclusive light absorption.

Chapter 2

Deterministic any-stacking-order and Suspended 2DM Transfer Procedure

In Chapter 1, we briefly presented the challenges encountered in the fabrication of 2D heterostructures [8, 10, 58]. We made the emphasis on the transfer of suspended 2DMs in the ultra-thin limit, such as one-atom-thick materials [59]. We also introduced the necessary theoretical background to understand the interaction of light with graphene.

This chapter describes, in detail, our transfer method and its capabilities to build NOEMS, among them, optical cavities. We begin with a comparison of the most widely-used stamping methods reported in literature and how our transfer method differs from them. A step-by-step demonstration of our nitrocellulose-based stamping procedure follows, showcasing its fabrication capabilities. Optical cavities with three distinct device geometries are fabricated with high yield: on-substrate, fully suspended and hybrid. We show how Raman spectroscopy can assess the quality of our devices, in terms of defect density, doping and uniformity of the stamped 2DM. Finally, a table with precise dimensions of all built devices is presented.

Deterministic and dry stamping transfer of any-stacking-order [14, 29, 26] and suspended ultra-thin 2D materials such as SLG and BLG have been out of reach so far. A first problem is that dry pick-up of naked (not encapsulated) 2DMs on SiO_2 substrates, permitting easy identification of thin exfoliated 2DMs [60], has not been possible due to the strong 2DM adhesion to SiO_2 [2]. Secondly, to deterministically

pick-up and transfer a single 2DM crystal while leaving nearby flakes untouched is challenging and best done with a three-dimensional micro-stamp [61]. Lastly, the stamping process of thin-suspended 2DMs requires great finesse to avoid tearing of the crystal, or collapse of the suspended 2DM due to capillary forces [34].

2.1 Comparing state-of-the-art stamping methods from literature

One way to transfer thin graphene crystals is to use a mechanical transfer method by vdW interactions [4] with hBN carrier films. The key aspect of this development is to provide easily detachable graphene crystals by growing them on Ge substrates. Due to a weak adhesion to this substrate, graphene can be effectively picked-up and transferred while being attached to a hBN film (see Figure 2.1). The transferred crystals are uniform and continuous with low defect density. [29]. This type of stamping method has its own limitations as it does not allow for the transfer of suspended nor naked crystals due to their encapsulation with the hBN carrier crystal. Other carrier films are used depending on the target crystal to be transferred. These methods fall in the category often called encapsulation.
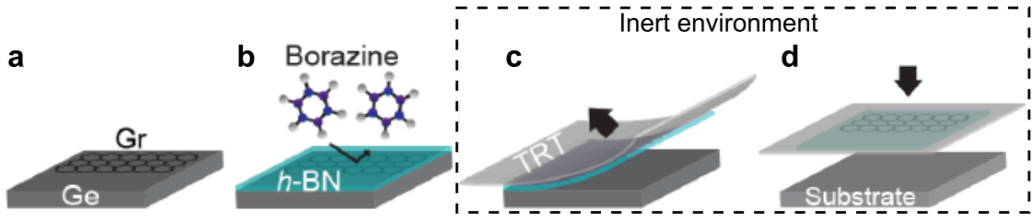
Figure 2.1: Schematics of the all-dry transfer process of graphene film by van der Waals interactions: (a) graphene growth on Ge(110), (b) h-BN growth, (c) mechanical exfoliation of h-BN/graphene hybrid film by thermal-release-tape (TRT), and (d) transfer of the film. Figure modified from [29].

To avoid encapsulation, we are required to use a material that can pick-up the 2D crystal and release it without leaving residues. A stamping transfer method that relies on the capillary forces of water-based solution to directly pick-up the crystal has been reported. The key concept of this technique is the utilization of a thin liquid film between a PDMS stamp and 2D crystals. The thin liquid film adheres

strongly to the 2DM and direct pick-up from its substrate is possible. As the liquid evaporates, the capillary forces holding the 2DM dissapear and release it (see Figure 2.2)[34]. The limitations of this method is the pick-up of several flakes at once, which complicates the deterministic transfer onto new substrates. This method cannot be used to suspend crystals due to the impractical, physical removal of the PDMS layer holding the 2D crystal.
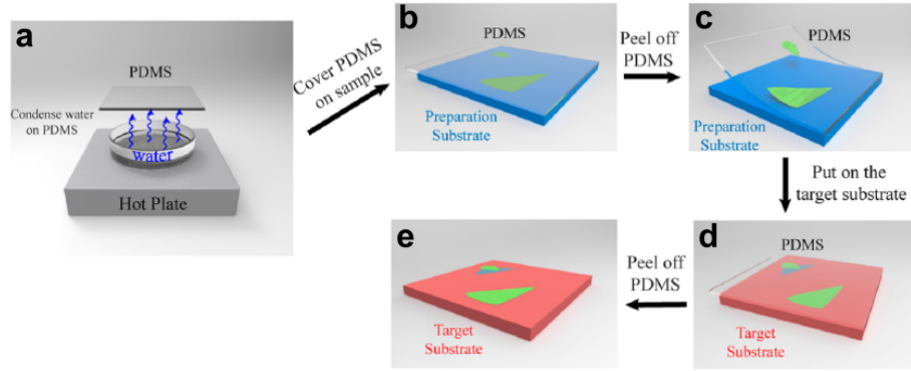
Figure 2.2: Schematic diagram of the capillary-force-assisted transfer procedure. (a) Condensation of (DI) water on a PDMS film. (b) The PDMS is gently placed aver the 2D crystals. (c) The PDMS is quickly peeled off from one side. (d) The crystal is now strongly adhered to the film. (e) The crystal is aligned on its new substrate. Figure reproduced from [34].

A different kind of stamping method that facilitates the fabrication of suspended and naked 2DMs, is called sacrificial layer. The conventional fabrication method for suspended graphene devices involves the exfoliation of graphene on SiO_2 substrates, followed by pattering of metal contacts to clamp the crystal. A subsequent wet etching of the oxide layer takes place in buffered hydro-fluoric acid. The release and suspention of graphene requires crytical point drying (CPD) [15]. This has device size limitations and is prone to collapse, making it a low yield method. There is a varied choice of sacrificial layer materials, which are normally polymers that can be etched or dissolved [40]. Using a polydimethyl-glutarimide (PMGI) based lift-off resist as the sacrificial layer instead of the conventional SiO_2 can increase the yield of suspended graphene devices. This method also requires clamping the graphene crystal with metal contacts before dissolving the sacrificial layer (see Figure 2.3) [37]. Limitations on the length of the suspended graphene channel are around 1 μm. There are simpler fabrication

methods, such as the exfoliation of 2DMs blindly performed on a patterned substrate, hoping some crystals will be suspended over pre-existing holes/trenches [16]. None of these methods is deterministic in nature and the characterization of the 2DMs can only be done once the heterostructure is completely assembled, making it impossible to compare the crystal quality before and after.
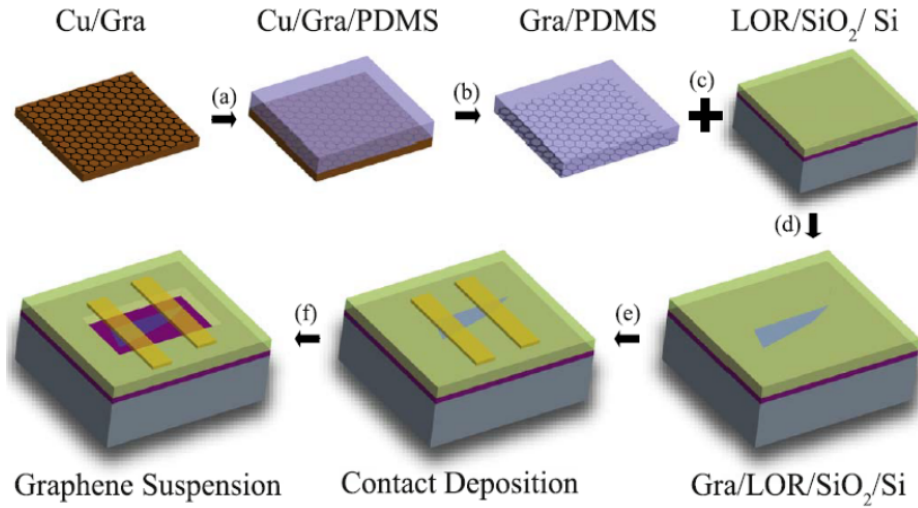
Figure 2.3: Schematic illustration of graphene suspension process. (a) Adhesion of Gr/Cu to PDMS. (b) Etching of the Cu. (c) Deposition of LOR onto SiO_2/Si substrate. (d) Attachment of graphene/PDMS to LOR/SiO_2/Si. (e) Metal contact deposition. (f) Suspension of graphene. Figure reproduced from [37].

2.2 Nitrocellulose-based Micro-Stamp Transfer Method

The stamping method is separated into five stages as shown in Figure 2.4. The first step consists in the preparation of a nitrocellulose micro-stamp and locating the desired 2DM crystal to transfer on a SiO_2 substrate. Secondly, the micro-stamp is then aligned above the 2DM and brought into contact. Later, the 2DM is picked-up from the SiO_2 substrate by carefully retracting the micro-stamp. The micro-stamp/2DM assembly is subsequently aligned above the new substrate and brought into contact. The transfer is completed with a facile microliter-volume solvent dissolution of the micro-stamp. We summarize the key details of each of these five stages below, and we briefly describe our stamping apparatus.
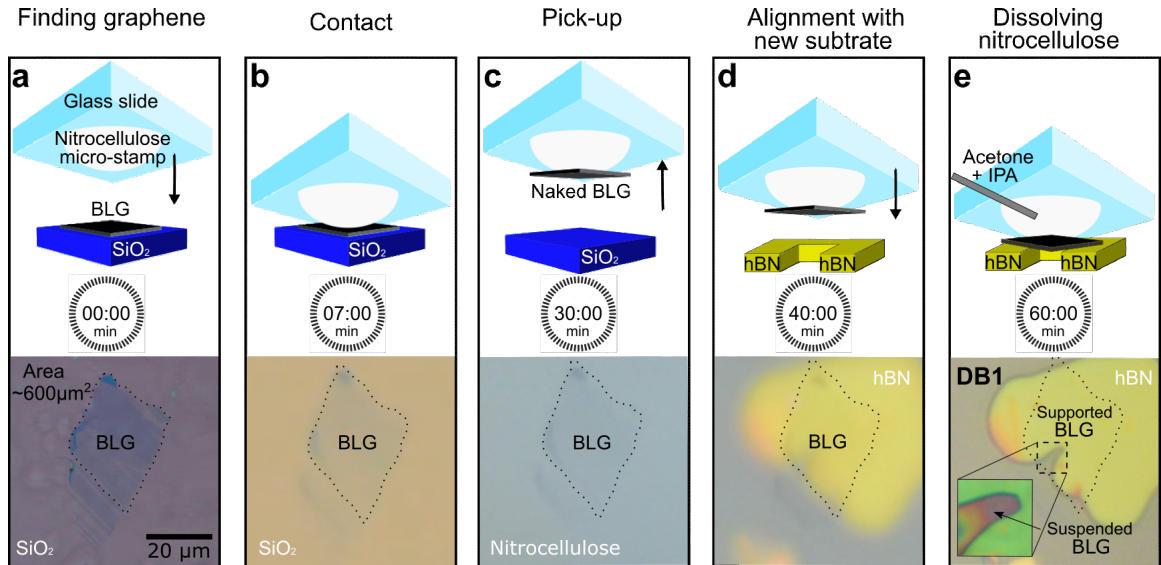
Figure 2.4: Step-by-step stamping process optimized for NOEMS assembly. (a) Locating the crystal to pick-up. Finding graphene crystal through highly transparent nitrocellulose droplet (b)Pressing the stamp on the crystal directly on a SiO_2 substrate. Making contact only with the desired crystal, and promoting adhesion. (c) Direct pick-up the 2D crystal from the SiO_2. (d) Micron-scale alignment of the naked 2D crystal on a new substrate. (e) Dissolving nitrocellulose stamp with a microliter droplets of acetone and isopropyl-alcohol, and controlled evaporation of solvents to favor crystal suspension.

Figure 2.4a shows a nitrocellulose-based micro-stamp positioned above a 2DM to

be picked-up. A fresh micro-stamp is prepared before each 2DM transfer, it has a roughly half-dome shape with x-y-z dimensions of 400-500 μm and its contact area during tranfer is limited to $\sim$ 200 μm x 200 μm. We prepare the micro-stamp by simply depositing a sub-microliter amount of nitrocellulose-based commercial solution (Extra Life^{TM} No Chip Top Coat - Revlon) on a glass slide, and letting it dry for approximately 6 minutes before making contact with the 2DM. We exfoliated 2DMs such as graphene, MoS_2, and hBN directly on SiO_2 to produce high-quality 2D crystals for transfer assembly. The micro-stamp preparation, substrate preparation, 2DM exfoliation procedure, and routine Raman characterization are discussed in the subsections below. The large BLG crystal visible at the bottom of Figure 2.4 is used to demonstrate the transfer procedure. In Figure 2.4b the micro-stamp is carefully aligned with the target crystal and brought into contact. The bottom of Figure 1b shows a top view through the transparent micro-stamp as it makes contact with the BLG crystal. The stamp only makes contact with the crystal and the immediate surrounding area. There is a sudden change in color from blueish to pinkish when the two make contact due to light interference. A single pressing down movement is required, to avoid deforming the micro-stamp and induce folding of the crystal [61]. The contact is maintained for $\sim$ 15 minutes to promote adhesion. In Figure 2.4c the micro-stamp is raised to pick-up the 2DM from the substrate. A key parameter to ensure a defect-free pick-up is to control the raising speed of the micro-stamp. We found that the nitrocellulose-based stamp acts as a hard surface at higher speeds (500 μm/s is ideal for thin 2DMs) and as a softer one at lower speeds (250 μm/s is ideal for thick 2DMs). In Figure 2.4d the target substrate or 2D heterostructure is placed underneath the micro-stamp/2DM assembly and aligned with micron precision. A representative alignment precision can be readily seen by comparing the contour of the BLG crystal in Figures 2.4d and 2.4e, and is found to be $\sim$ 2 μm. Once the BLG crystal is aligned atop a hBN/SiO_2 heterostructure, the stamp is lowered to transfer the BLG on the hBN substrate, which includes a trench on its side allowing suspension of the BLG. Figure 2.4e shows how after gently pressing the micro-stamp/2DM against the target substrate, the stamp is controllably dissolved with microliter-volume acetone and isopropyl alcohol (IPA) to cleanly transfer the 2DM. To dissolve the micro-stamp, a micro-pipette is used to insert acetone in the spacing between the glass slide anchoring the micro-stamp and the hBN substrate. The acetone rapidly

dissolves the droplet, which can be easily monitored in real time, and releases the graphene. Once the droplet is dissolved, we raise the glass slide by ~ 150 μm and use the same pipette to flush with isopropyl alcohol. We repeat this acetone/alcohol flushing to clean residues of both the micro-stamp and acetone. At this point the 2DM has been transferred to the substrate/heterostrcuture, but is submerged in an IPA solution (lower-surface tension than acetone). For transferring suspended crystals, we control the evaporation rate of IPA to avoid their collapse due to capillary forces. By raising or lowering the glass slide we can expose more or less of the solution to the atmosphere and control the evaporation rate (see subsection, Transfer:Solvent dissolution of micro-stamp). It permits a delicate transfer of suspended 2DMs, such as the suspended BLG region in Figure 2.4e. The complete transfer procedure can be visualized in the Movie 1 (link in the appendix).
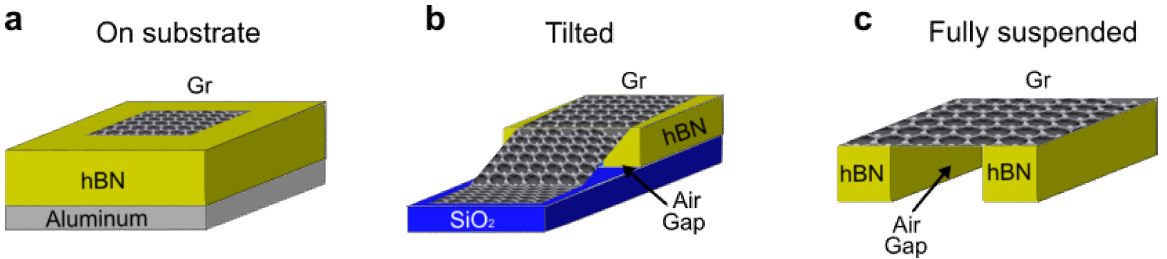
Figure 2.5: Device geometries. (a) Geometry of our stamped fully-supported heterostructure optical cavities. (B) Geometry of our stamped tilted suspended NOEMS. (c) Geometry of our stamped fully-suspended NOEMS.

Figures 2.5 a-c show the three main heterostructure geometries we fabricate and discuss in the rest of this work, (f) BLG/hBN/Al heterostructures (g) tilted-suspension BLG/air(variable thickness)/SiO2, and (h) full-suspension BLG/air/SiO2.

2.2.1   Stamping Apparatus with x-y-z-θ Alignment

The stamping setup used is shown in Figure 2.6 below. It consists of a rotating stage with a vacuum system to hold the substrate in place, a tree-axis micro manipulator (x, y and z-axis) that holds the glass slide with the micro-stamp (droplet), a long working distance optical assembly attached to a high resolution CCD camera which is connected to a monitor for live viewing. This setup is based on previous stamping techniques, often called deterministic transfer [10] [1] [31] [62]. Most of our micro-stamp transfer process is all-dry, and only requires micro-liter amounts of mild

solvents (acetone and IPA) at the end of the process.
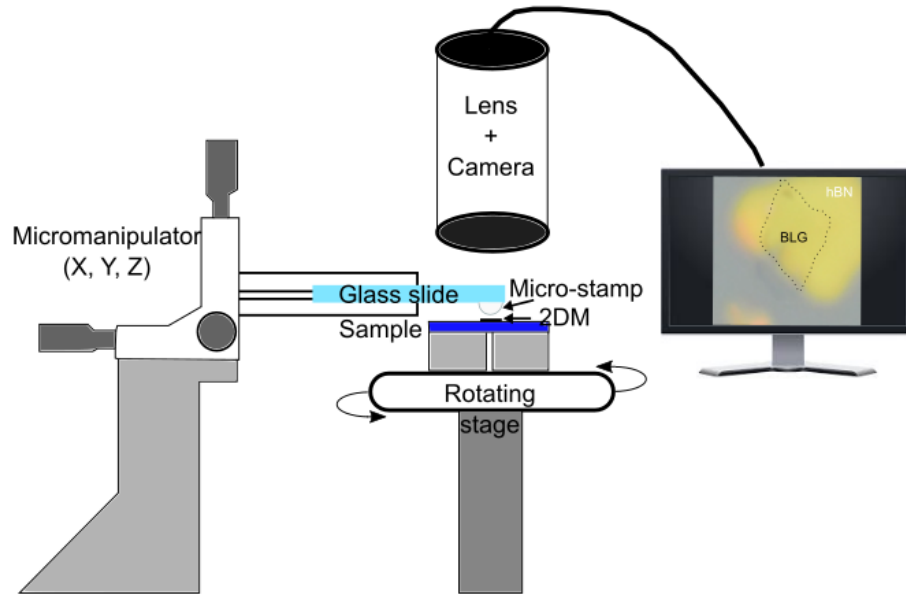
Figure 2.6: Stamping apparatus. The substrate with the 2DM-to-be-transferred is placed on a rotating stage and held by vacuum, while a glass slide with a custom micro-stamp is attached to the x-y-z manipulator. A long working distance optical assembly is connected to a digital camera which displays a live view of the transfer process.

2.2.2 2DM Exfoliation

To exfoliate graphene crystals, we start with high quality HOPG graphite flakes (Kish Graphite B from Covalent Materials Corporation). To exfoliate hBN 2D crystals, we start with high quality hBN crystals (PT110 Powder CTR from Momentive Performance Materials). To exfoliate MoS_2 crystals, we start with a Synthetic MoS2 crystal from 2D Semiconductors. Our wafers are made of 500 μm-thick of Si with a 310 nm-thick SiO_2 film on them. We transfer a photolithography-patterned coordinate grid on these substrate, to easily locate the candidate 2DM crystals to be stamped. To exfoliate our 2DMs, we first do a coarse mechanical cleavage with a razor blade to generate the thinnest flake possible. We then place these flakes on a piece of scotch tape (exfoliation of hBN is done using "Nitto" tape) where further cleavage is done by repeated folding the scotch tape [63]. Before transferring the exfoliated 2DM from the scotch tape to the SiO_2/Si substrate, we lightly etch the substrate with a dilute hydrochloric acid (HCl) and hydrogen peroxide (H_2O_2) solution (18:1:1) at 75 C° for 5 minutes, to get rid of any surface residues. This etching minimizes the substrate contamination and promotes adhesion between 2DM crystals and the oxide. The substrate is carefully rinsed with DI water, blown dry with nitrogen and baked at 120 C° for 2 minutes to evaporate any water left. The tape containing the 2DM flakes is gently pressed with a finger on the substrate, and we wait for about 10 minutes before slowly peeling off the tape (0.1 mm/s) with the help of tweezers.

We locate and characterize the crystals on the substrate with an optical microscope and Raman spectroscopy. For the successful deterministic transfer of ultra-thin 2DMs (e.g. SLG, BLG), we found empirically our best results when respecting a lower limit on the crystal surface area of at least 5 by 5 μm, as well as a upper time limit of 3 days after the exfoliation was performed. We did not identify any upper limit on the crystal surface area. The scotch tape itself leaves organic residues that need to be cleaned before the deterministic transfer (see Figure 2.7). The substrate with exfoliated 2DM is submerged in a warm bath of acetone at 75 C° for 5 minutes, rinsed with IPA, then with DI water and baked at 120 C° for 2 minutes. The substrate is then mounted on the vacuum stage of the stamping apparatus (Figure 2.6) and the lens and camera system is focused on the target crystal.
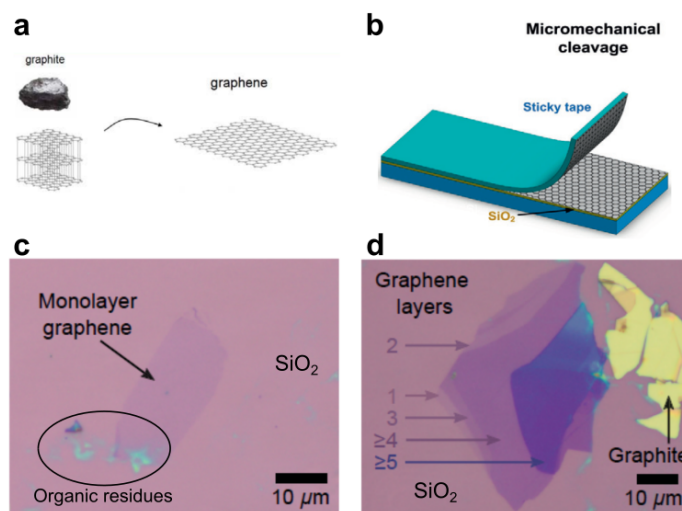
Figure 2.7: Exfoliation of graphite. (a) Graphene exfoliated from a graphite crystal. (b) Schematic illustration of micromechanical cleavage by the so called "Scotch Tape". Reproduced from [63].(c) Exfoliated SLG on SiO_2/Si substrate, organic residues from the tape adhesive are present in the bottom of the crystal. (d) Graphene crystal with regions of different number of layers identified by their color contrast.

2.2.3 Micro-Stamp Preparation

Previous deterministic transfer methods have used stamps based on materials such as polymethyl methacrylate (PMMA) [31], thermal release tape (TRP) [36], polyvinyl alcohol (PVA) and polypropylene carbonate (PPC) [14] [64]. Our stamp is made with a commercially available product (Extra Life™ No Chip Top Coat - Revlon). The ideal micro-stamp shape is close to a half-ellipsoid (Fig. 2.8c). The size and shape of the micro-stamp determine the contact area between the stamp and 2DMs. The optimal stamp size for our work was around 400 μm x 600 μm x 400 μm, with a contact area (top of stamp) of approximately 200 μm by 200 μm. To achieve these micro-stamp dimensions, we first submerge the needle of a 1 mL syringe, into a small drop of the solution deposited on a glass slide (Fig. 2.8a). By capillary forces a small drop will stay on needle when pulled away from it. When the needle barely touches the target clean glass slide, it transfers an even smaller droplet on its surface (Fig. 2.8b). The resulting micro-stamp is inspected by optical microscopy to make sure that it has the target shape and size. The narrow apex of the droplet appears as a bright spot in Fig. 2.8c. This process only takes a few minutes and is very reproducible.
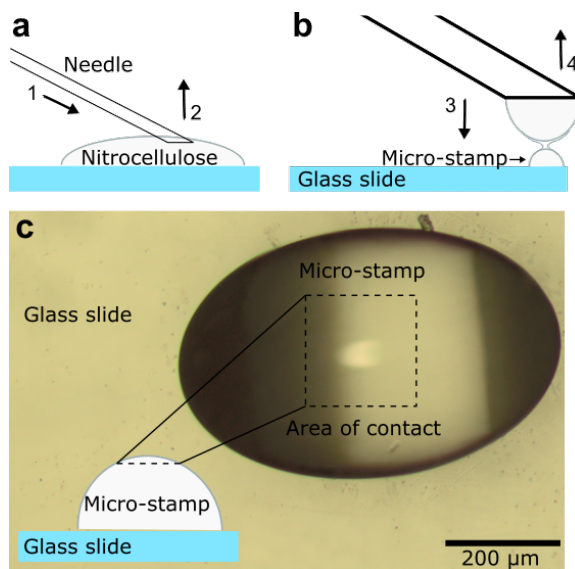
Figure 2.8: Nitrocellulose micro-stamp preparation. (a) A sharp needle is submerged in a drop of nitrocellulose-solution (Extra Life^{TM} No Chip Top Coat - Revlon), and then pulled up so that a small droplet remains attached to the needed by capillary forces. (b) A slight contact of the droplet with the target glass slide leaves a reproducible micro-stamp. (c) Top-view optical image of a typical micro-stamp, whose top gives a 200 μm x 200 μm contact area for 2DM pick-up. Inset: Illustration of the micro-stamp profile.

2.2.4   Making Contact Between Micro-Stamp and Crystal

The glass slide with the micro-stamp is mounted on the micro-manipulator, the apex of the stamp is centred 1 mm above the crystal selected for pick-up (the micro-stamp is highly transparent and acts as a lens due to its ellipsoidal shape). The stamp is left to dry for 10 ± 3 min. During this time the stamp (droplet) surface hardens. After that time the stamp is lowered slowly (~ 50 μm/s) to contact the selected crystal for pick-up and its immediate surrounding area (~ 4000 μm^2). The stamp suddenly changes in the color (pinkish) when contact is made. The contact must be done on the first trial, otherwise the micro-stamp deforms and the pick-up process may induce crystal folding or not work reliably. The stamp-2DM contact is maintained constant for about 20 ± 5 min. to promote strong adhesion. These parameters are the same for all of the 2D crystals we transferred: SLG, BLG, FLG, hBN and MoS$_2$ crystals.

2.2.5   Pick-up of naked crystal

The pick-up speed of the micro-stamp/2DM assembly away from the original substrate is controlled with the z-axis of the micro-manipulator. The optimal speed depends on the thickness of the crystal. We found that the nitrocellulose-based stamp acts as a hard surface at high speeds and as a flexible one at lower speeds. The vertical pick-up speed for atomically thin crystals (SLG, BLG and few layers) is around 500 μm/s, while for thicker crystals it is reduced to ~ 250 μm/s. The live view option of the camera allows us to observe when the crystal is completely picked-up and if the process induces crystal folds. Once the crystal is picked up (Fig. 2.9), we raise the stamp by an additional 500 μm, and exchange the old SiO$_2$ substrate with the new target substrate. In summary, the strong adhesion of our micro-stamp with 2DMs is able to overcome the vdW interactions between these 2DMs and SiO$_2$ [34].
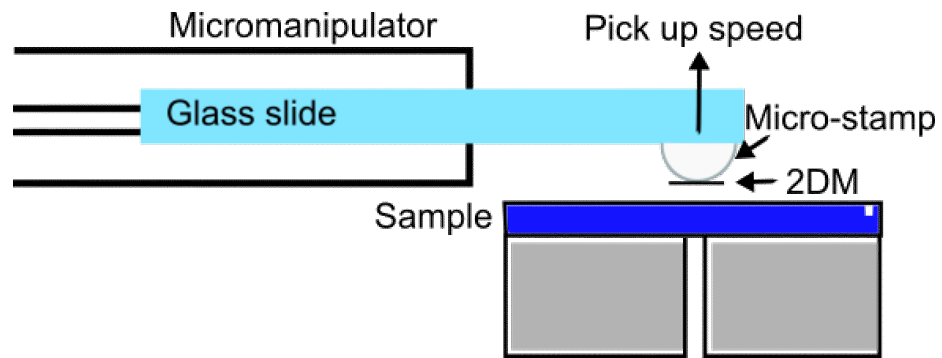
Figure 2.9: Schematic of the 2DM pick-up process from SiO_2 substrate. A micro-manipulator holds the glass slide to which the micro-stamp is attached. By raising the slide, the 2DM is cleanly picked-up from the SiO_2 substrate.

2.2.6 Alignment with new substrate

We often use hBN as the target substrate for transfer, but also used successfully SiO$_2$, graphene, or Aluminium as target substrates. Exfoliated hBN crystals on SiO$_2$ substrates often exhibit "U" shape edges which can be used as a naturally occurring trenches ideal for transferring suspended 2DMs. We first characterize hBN or any other substrates via AFM (thickness, shape, flatness). Then, we place the target substrate on the stamping stage, focus the optical assembly on the substrate. We mark (trace) the substrate crystal (e.g. hBN) contour on the video screen for future reference. The 2DM-substrate alignment is done in successive steps. First, the micro-stamp is centered and positioned about 0.5 mm above the target substrate, the substrate is aligned as desired relative to the 2D crystal orientation on the micro-stamp. In a second stage, we focus the image right above the substrate and lower progressively the 2D crystal at about 20 μm/s until both substrate and 2D crystal are clearly visible in focus. A final alignment correction is done before bringing them into gentle contact at about 5 μm/s. We stop lowering the micro-stamp when it contacts the target substrate (or target heterostructure). We ensure that the micro-stamp is not pressed hard enough to deform and touch beyond the immediate surroundings of the 2DM.

2.2.7 Transfer: Solvent Dissolution of Mircro-Stamp

A clean micro-pipette is used to inject one drop of acetone (500 μL) in the spacing between the micro-stamp and the substrate (Fig. 2.10a). The acetone rapidly dissolves the stamp (this can be monitored in real time on the screen) and releases the 2D crystal. Once the droplet has been dissolved, we raise the glass slide by 500 μm and do a local rinsing with IPA using the same micro-pipette. We repeat a couple of times the rinsing with IPA to completely flush the acetone and polymer residues (Fig. 2.10b). At this point the 2D crystal has been transferred on the new substrate and is submerged in the IPA solution (Fig. 2.10c). To transfer suspended crystals, we need to control the evaporation rate of IPA to avoid their collapse due to capillary forces. The evaporation rate is easily tuned by raising or lowering the glass slide to tailor the exposure of the IPA solution to the atmosphere (Fig. 2.10d). This procedure removes the need for critical point drying of our suspended 2D heterostructures when the height of suspension is above 500 nm. It enables the stamping of defect-free

suspended crystals with a simple table-top apparatus.
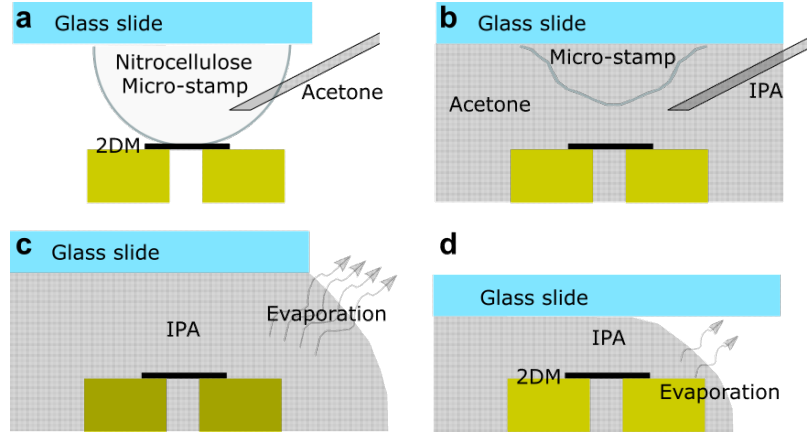
Figure 2.10: Transfer: Solvent dissolving of micro-stamp to free up the 2D crystal. (a) A micro-pipette is used to introduce a drop of acetone. (b) The acetone starts to dissolve the stamp and the 2D crystal is freed up, a couple of IPA drops are injected to flush the acetone and polymer residues. (c) The stamp is completely dissolved, and fast evaporation of the solvent starts to occur. (d) By the lowering of the glass slide we decrease the rate of evaporation, minimizing the risk of crystal collapse.

2.3 Dry Pick-up directly from SiO_2 and any-stacking-order 2DM transfer

In Figure 2.11, we present high-quality and large area 2D heterostructures including graphene, hBN, and MoS_2 assembled following the procedures in Figure 2.4. The optical images showcase the ability to dry pick-up of naked and large area 2DMs from SiO_2, and deterministically transfer them into any-stacking-order heterostructures. Both the optical and Raman data presented confirm a low-defect density in the transferred crystals. To assemble the heterostructures visible in Figures 2.11a,c,e, we first evaporated a 50nm-thick film of Aluminum (highly reflector material) on a SiO_2/Si wafer, which will act as the back-plane mirror of an optical cavity as discussed later in chapter 3. The next step was to deterministically transfer thick (~ 400 nm) and large area hBN crystals (up to ~ 1000 m^2) which will act as substrates for the ultra-thin crystals, and define the thickness of the optical cavity heterostructures. We then deterministically selected and picked-up large area 2DM crystals from a SiO2 substrate, as visible in the Figures 2.11a,d,g. These large area crystals (few hundred

μm^2) include ultra-thin regions such as SLG, BLG, few-layer graphene (FLG), and few-nm thick MoS$_2$. We note that the entire area of these large target crystals was transferred without tearing or folding, and very few small bubbles are visible in the transferred crystals. Out of the 21 on-substrate heterostructure assemblies we attempted, 20 were successful as shown in Figure 2.11.

The Raman data shown in Figure 2.11c,f,i were taken at the red-marker locations shown in the corresponding optical images (before label refers to the inset optical images, after label refers to the main panel optical images). We remark that, as expected, the relative height of the Raman peaks, such as the G and 2D peaks in graphene, are affected after the assembly of the optical cavity heterostructures. The ratio between the G and 2D peaks also changes and is dependent on the device geometry [48]. However we can readily see that the width of the Raman resonances are the same before and after transfer of the ultra-thin crystals, moreover there is a neglible D-peak in the graphene spectra, indicating that no major microscopic disorder was introduced during the stamping [55, 56, 34, 74].
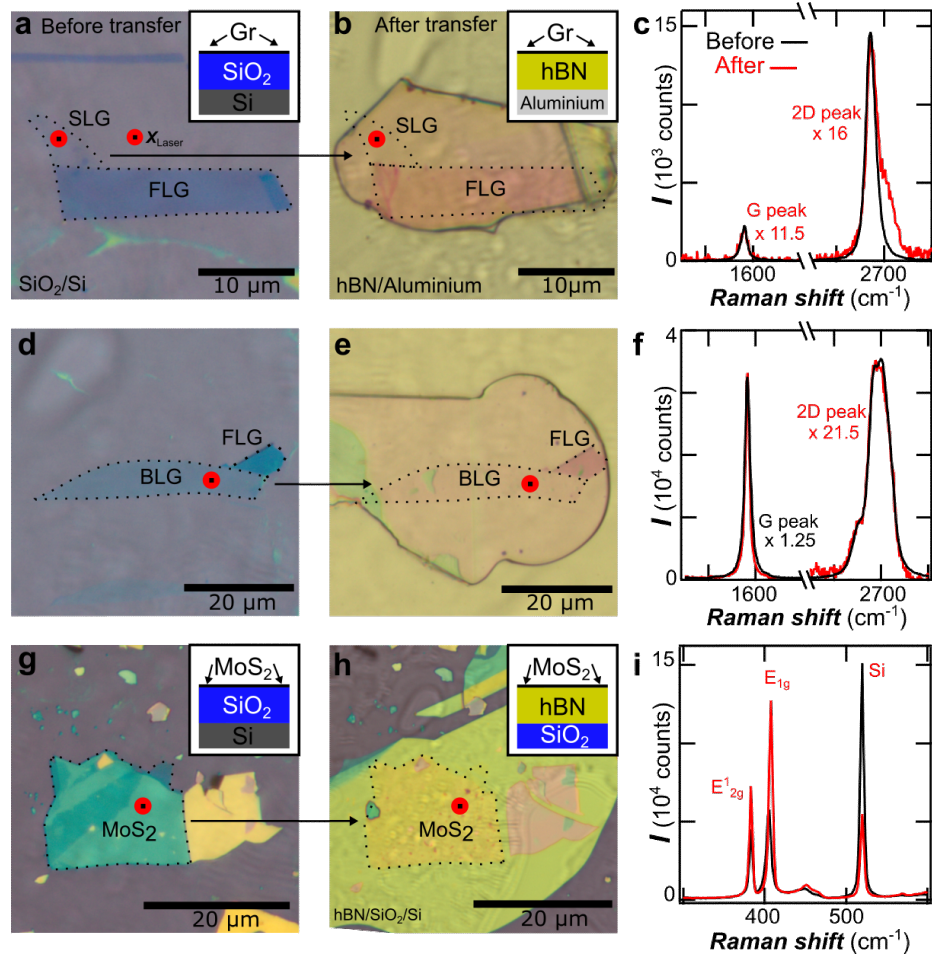
Figure 2.11: On substrate devices with different 2DM and thickness. (a) Optical image of SLG crystal before and (b) after stamping, red dot is the location of the Raman scan. Insets: Illustrations of device profile. (c) Raman spectrum before (black) and after (red). (d) Optical image of BLG crystal before and (e) after stamping. (f) Raman spectrum before and after. (g) Optical image of MoS_2 crystal before and (h) after stamping. Insets: Illustrations of device profile. (i) Raman spectrum before and after.

Figures 2.12a-b display how we can not only align 2DM atop of each other but also controllably position two 2DMs at relative x-y positions. Two separate transfer procedures were used to pick-up two hBN crystals (inset of Figure 2.12a) from SiO_2 substrates and transfer them both to another SiO_2 substrate to fabricate a narrow hBN trench, as shown in Figure 2.12a. The details of the trench are shown in Figure 2.12b, and the quality of the both the rotational (one degree precision) and translational (one micro precision) alignment are clearly visible. Such trenches can be used for subsequent NOEMS assembly by stamping a 2DM on top of the trench as we will see next.
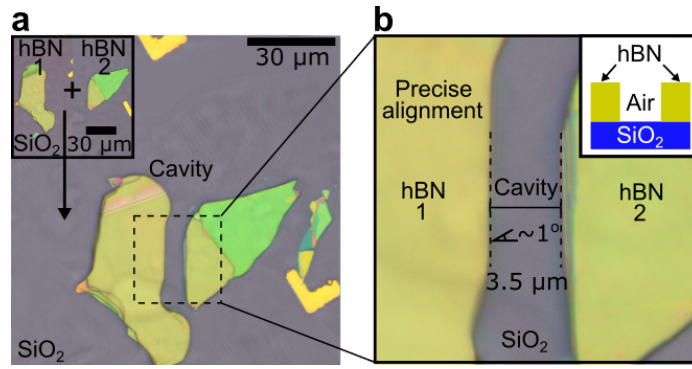
Figure 2.12: Alignment precision. (a) Two relatively large-area hBN crystals brought together by our deterministic transfer process to form a micro-cavity. Inset: hBN crystals on their former substrates. (b) Zoom in the cavity region, its length is 3.5 μm. Inset: Diagram of device.

2.4 Facile Stamping of Ultra-thin Suspended 2DMs

Devices of tilted geometry are a hybrid where both sides of a BLG crystal are supported at different heights while the middle part is suspended. In Figures 2.13a,b we show top view optical images of two such devices, where we find four distinct regions. In Region I, the BLG crystal is supported on a SiO_2 substrate, in region II it is suspended (varying air-spacer thickness), in region III it is fully suspended (approximately constant) ,and in region IV it is supported on a hBN/SiO_2 substrate. The stability of such devices is short-lived as the distance between the 2D crystal and SiO_2 substrate decreases until it reaches a configuration where most of the crystal is

collapsed. This can be seen in Figures 2.13b-c, in Fig. 2.13b the suspended crystal area (regions II and III) is greater than the crystal area supported on SiO_2 (region I). In Fig. 2.13c we show the AFM of the same device a couple days later, region I (black) now covers most of the cavity. A measurement of the crystal suspension height is shown in Fig. 2.13d, it varies continuously from 0 to ~ 360 nm.
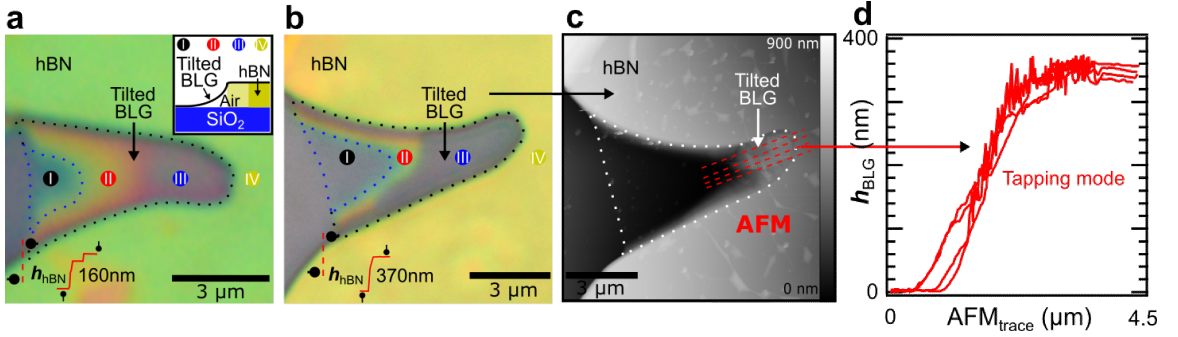
Figure 2.13: Tilted BLG devices. (a) Optical image of a tilted BLG with varying air-spacer thickness from 0 to 160 nm. Inset: Illustration of the device profile. (b) Optical image of a tilted BLG with varying air-spacer thickness from 0 to 370 nm. (c) AFM image of (b) with traces in dotted red lines. (d) Plot of BLG suspension height as a function of AFM trace position. Both devices have four distinct regions, I and IV on substrate and II and III suspended.

Figure 2.14 shows three examples of thin-suspended graphene heterostructures assembled following the procedure in Figure 2.4. The optical and Raman data show these thin-suspended 2DMs were transferred without tearing, folding or the introduction of microscopic disorder, precisely aligned, are suspended in close proximity above a substrate (down to 550 nm) without critical point drying, and have suspended areas up to ~ 15 μm^2. Figure 2.14a shows a top view of a FLG/air/SiO_2 structure (right inset: side-view diagram) resulting from the transfer of large area FLG flake (left inset) atop of large hBN exfoliated crystal with a U-shaped cavity. Such cavities naturally occur during hBN exfoliation and offer lithography-free trenches for graphene suspension. Figure 2.14b shows the Raman data acquired at the same location (red marker) on the FLG crystal before and after suspension. While the relative height of the Raman resonances changes before/after due to the interferences from the underlying heterostructure, as discussed before, the width of the resonances remain the same and no D-peak is visible after suspension. Figure 2.14c shows a top view of a transferred BLG/air/SiO_2 structure, resulting from the suspension of a large area BLG crystal (inset). Figure 2.14d presents the Raman data recorded

(red marker) after the suspension, showing negligible D peak. Similarly Figure 2.14e shows a top view optical image of suspended $SLG/air/SiO_2$ heterostructure and the inset shows the same crystal on SiO_2. Figure 2.14f presents the Raman data recorded (red marker) after the SLG suspension, showing negligible D peak. All ratios between the D and G peaks are much less than 1 in our fabricated heterostructures, defected graphene samples have a ratio close or greater than 1 [55].
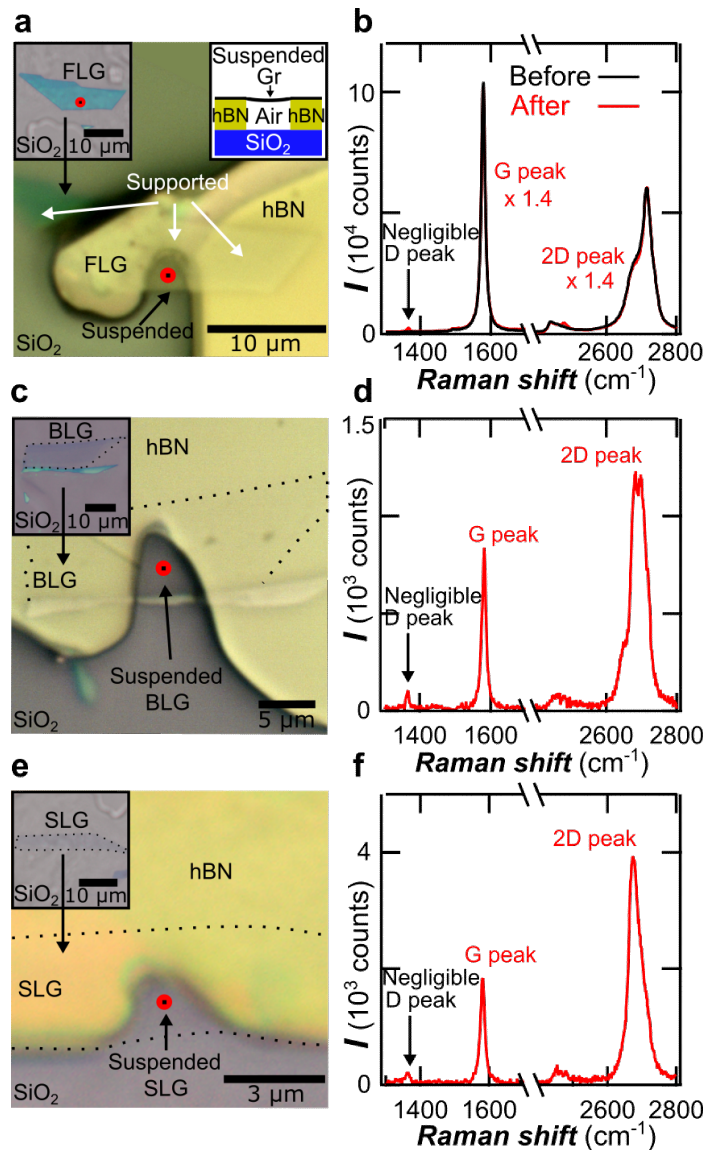
Figure 2.14: Graphene-based suspended heterostructures. Optical images of freely suspended (a) FLG (Right inset: Side view diagram), (c) BLG and (e) SLG crystals over a hBN trench. Left insets: Same 2D crystals before suspension. (b),(d),(f) Raman data acquired in the location of the red marker, showing negligible defect-related D peak.

Figure 2.15a shows an AFM image of a suspended SLG/air/SiO$_2$ heterostructure, confirming a uniform suspension of the SLG and the red trace in the bottom left is an AFM data trace showing the height of the crystal suspension around 550 nm. This low and uniform suspension height is an important figure of merit for the fabrication of NEMS and NOEMS, since this height controls the electrostatic gating effectiveness of the suspended graphene [65]. Figure 2.15b shows a SEM image with an inclination angle of $\sim 70°$ of a suspended BLG. The top right inset shows the integrated area (number of scattering events) under the G-peak as a function of laser power on the suspended BLG. The linear relationship confirms that the suspended crystal does not significantly heat up at the modest laser power (≤ 6 mW/μm^2) we used for our Raman data acquisitions.
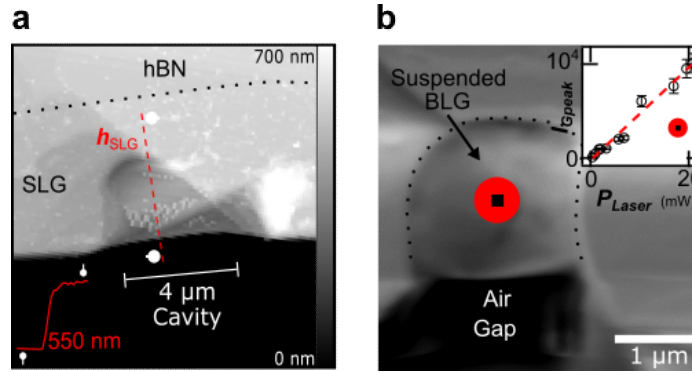
Figure 2.15: Fully suspended SLG and BLG NOEMS. (a) AFM image (tapping mode) of a freely and uniform suspended SLG over a 4 μm long hBN trench. (b) Tilted SEM image of a suspended BLG crystal. Inset: Integrated Raman scattering intensity of the G peak, taken at the location of the red marker in the suspended BLG.

Out of the 15 suspended heterostructure assemblies we attempted, 14 were successful as those shown in Figure 2.14, and more details are provided in the next section. This deterministic, facile, and flexible suspended heterostructure fabrication can facilitate the development of many NEMS and NOEMS applications in optoelectronics, twistronics. We demonstrate a first use of this fabrication route to assemble heterostructures able to widely increase or suppress how much visible light energy is absorbed (i.e. light-matter interactions) in BLG.

2.5 Results of our Deterministic Transfer Method

In Figure 2.14, we describe the capabilities of our method to transfer naked (not encapsulated) 2DM crystals with direct dry pick-up from SiO_2. We created on-substrate heterostructures with deterministic and precise alignment of large 2D crystals. Below, we present in Table 2.1 a detailed list of our 21 attempts at transferring 2DM crystals from a substrate to another substrate following the exact recipe presented in section 2.2 and Figure 2.4 of this chapter. For each device listed in Table 2.1, we acquired high quality optical images of the 2DM before and after the transfer as shown in Figure 2.16 for two large area 2DM crystals. These optical images were used to extract the surface area of the crystals listed in Table 2.1, and to verify that no significant macroscopic damage (tearing, folding, and bubbles) was introduced during the transfer. Before and after the transfer we also acquired multiple Raman scans (along the red lines in Figure 2.16) and AFM (tapping mode) images of the devices. The comparison of the Raman spectra (Figure 2.11) before and after transfer confirmed that no microscopic disorder was introduced during the transfer. The alignment accuracy of the deterministic transfer was down to two μm when great care was taken. We successfully transferred all of the materials we tried, and which include various thicknesses of graphene (SLG, BLG, TLG, FLG), MoS_2, and hBN. Table 2.1 also details the thickness of the materials transferred and the final heterostructures created. The transfer procedure was very reproducible and its success rate was very high. Out of the 21 attempts, there was only 1 failure (no transfer) and 2 partial successes (partial tearing of the crystal), and 18 completely successful transfers. In terms of producing the desired planar heterostructures, we thus find the success rate to be around 95%.
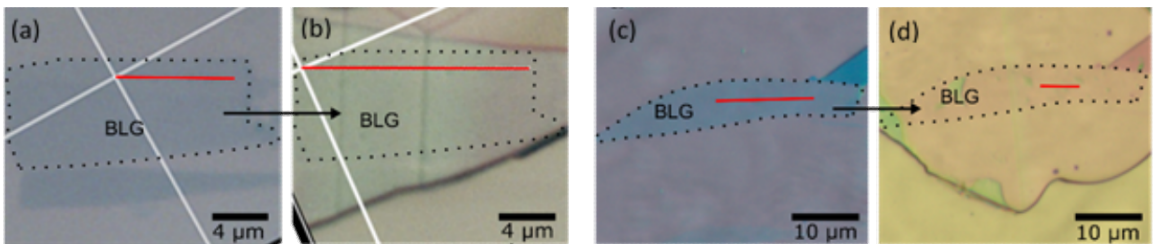
Figure 2.16: Large area BLG crystals before and after transfer. Raman scan in red lines. (a),(c) BLG before transfer, supported on a SiO_2 susbtrate. (b),(d) BLG after transfer, supported on a hBN/Aluminium substrate

Device	Pre-area (μm^2)	Post-area (μm^2)	Material	Structure
SA1	15	15	SLG	SLG/hBN/Al
SA2	25	25	SLG	SLG/hBN/Al
BA1	140	140	BLG	BLG/hBN/Al
BA2	50	25	BLG	BLG/hBN/Al
BA3	60	15	BLG	BLG/hBN/Al
BA4	190	190	BLG	BLG/hBN/Al
BA5	20	20	BLG	BLG/hBN/Al
BA6	40	40	BLG	BLG/hBN/Al
BAX	90	0	BLG	Failed
TA1	350	350	TLG	TLG/hBN/SiO$_2$
FA1	50	50	FLG	FLG/hBN/SiO$_2$
FA2	360	360	FLG	FLG/hBN/SiO$_2$
FA3	670	670	FLG	FLG/hBN/SiO$_2$
MoA1	290	290	FL MoS$_2$	MoS$_2$/hBN/SiO$_2$
MoA2	120	120	10nm MoS$_2$	MoS$_2$/hBN/SiO$_2$
BNA1	1150	1150	110nm hBN	hBN/SiO$_2$
BNA2	580	580	610nm hBN	hBN/SiO$_2$
BNA3	450	450	960nm hBN	hBN/SiO$_2$
BNA4	550	550	1250nm hBN	hBN/SiO$_2$
BNA5	290	290	1500nm hBN	hBN/SiO$_2$

Table 2.1: List of on-substrate devices. Device means device name. Pre-area and Post-area are the crystal area before and after tranfer. Material is the 2DM and its thickness. Structure is the final heterostructure composition. Devices SA1-2, BA1-4, MoA1 and BNA1 are shown in this thesis.

In Figure 2.14 of this chapter, we describe the capabilities of our method to transfer suspended ultra-thin 2DM crystals on hBN trenches with alignment, and without any need for critical points drying. We created suspended SLG, BLG, and FLG suspended heterostructures with various suspensions heights, including some structures with a variable (tiltled) suspension height as shown in Figure 2.13. Below, we present in Table 2.2 a detailed list of our 15 attempts at transferring 2DM crystals from SiO$_2$ substrates to hBN trenches for suspension. We followed the exact recipe presented in Section 2.2 and Figure 2.4 of this chapter. For each device listed in Table 2.2, we acquired high quality optical images of the 2DM before and after the transfer, as well as SEM images after suspension, as shown in Figure 2.15b for a suspended BLG heterostructure, with a uniform suspension height. Figures 2.13a,b

show two devices with a titled-suspension geometry to achieve a continuous variation of its suspension height. These images, and others, were used to extract the surface area of the crystals listed in Table 2.2, and to verify that no significant macroscopic damage (tearing, folding, and bubbles) was introduced during the transfer. All the suspended heterostructures created were stacked as graphene/air/SiO$_2$. In order to determine the suspension height of graphene, and the absence of wrinkles introduced during transfer, we used tilted-SEM imaging and AFM imaging (tipping mode) after suspension, as shown in Figure 2.17. It showed uniform suspension height (except in the tilted devices), and this suspension height was further confirmed by the Raman spectra vs. position presented later in Chapter 4. These measurements of the Raman factor are highly sensitive to the suspension height of the graphene [66].
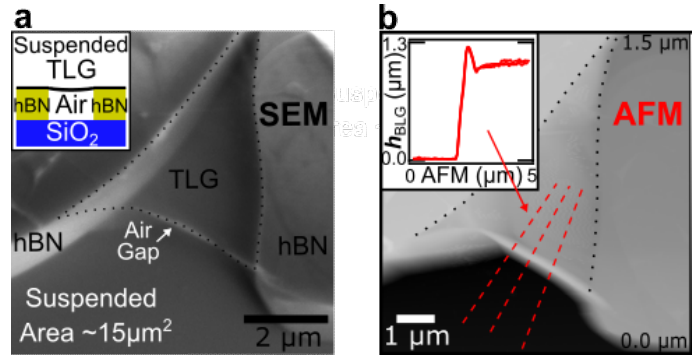
Figure 2.17: Transferred suspended trilayer graphene heterostructure. (a) Tilted-SEM image showing a uniform and wrinkle-free suspension. Inset: diagram of the heterostructure geometry. (b) AFM image of the same suspended trilayer-graphene device. The inset shows the line cuts along the dashed red lines, and a uniform suspension height.

The transfer procedure was very reproducible and its success rate was very high. Out of the 15 attempts, there was only 1 failure (transferred, but no suspension) and 14 completely successful transfers. In terms of producing the desired suspended heterostructures, we thus find the success rate to be around 93%.

Dev.	Pre-area (μm^2)	Susp-area (μm^2)	Supp-area (μm^2)	Mat.	Height (nm)
SC1	90	8	82	SLG	550
SC2	210	12	198	SLG	520
BC1	620	4	616	BLG	1340
BC2	250	12	238	BLG	1150
BB1	370	9	361	BLG	360 (tilted)
BB2	600	12	588	BLG	160 (tilted)
TC1	170	6	164	TLG	570
TC2	110	15	95	TLG	1050
FCX	650	0	650	FLG	Failed
FC1	100	8	92	FLG	1300
FC2	140	8	132	FLG	1900
FC3	160	7	153	FLG	1100
FC4	190	3	187	FLG	900
FC5	100	6	94	FLG	1350
FC6	70	7	63	FLG	340

Table 2.2: List of suspended devices. Dev. means device name. Pre-area is the crystal area before tranfer. Susp-area is the suspended and Supp.area is the on-substrate crystal area after transfer. Mat. means material, e.g. SLG, BLG. Height is the crystal suspension height. Devices SC1-2, BC1-2, BB1-2, TC1 and FC2 are shown in this thesis.

Chapter 3

Tuning of Graphene's Raman Factor and Light Absorption

The necessary theory, a detailed description of our stamping transfer process and the fabricated 2DM heterostructures were presented in the previous chapters. We discussed the two main optical processes involved; Raman scattering and its underlying light absorption [52, 46, 48]. These two are the basis for the theoretical models used in this chapter to describe the optical measurements performed on the fabricated graphene-based optical cavities. This chapter reports the ability to tune the graphene exclusive light absorption via the manipulation of its Raman scattering intensity in several stamped devices. Two models based on first-principles calculations are used to explain our results. We detail the instrumentation and calibration process used to perform our optical microscopy measurements. The procedure to extract the BLG exclusive absorption from Raman scattering intensity follows. Finally we report the tuning of the BLG Raman scattering intensity by a factor of up to 19 and the exclusive light absorption by a factor up to 18.

Developing 2DMs for optoelectronics applications [8] or exploring 2D light-matter interactions [12] requires increasing the very small bare light absorption in ultra-thin 2DMs [24]. Planar 2D heterostructures can act as optical interferometric cavities to greatly enhance light absorption and Raman scattering in 2DMs, including graphene [21, 66, 7, 19] and 2D transition metal dichalcogenides [20]. While previous work focused on maximizing absoprtion of the infrared range [21, 67], and on-substrate 2DMs, we focus on both on visible light and on suspended BLG. We

demonstrate that quantitative light absorption enhancement is feasible in suspended 2D heterostructures, and could lead to high on-off ratio light-absorption transducers. This will open up opportunities to generate strong light-matter interactions in 2D NEMS [19], and specifically for BLG and twistronics [7] NOEMS.

3.1 Modeling Raman Factor and Exclusive Light Absorption in Graphene Heterostructures

There is a strong interest in enhancing the light absorption of graphene [21] and 2D TMDs [19] to optimize their great potential for light harvesting applications [68], and also to develop new tools for NOEMS research [12]. The Raman scattering intensity in an isolated 2D crystal is linearly proportional to light absorption since only a tiny fraction of photons undergo Raman scattering [48]. Both the light absorption and Raman scattering intensity in planar heterostructures can be enhanced via constructive and destructive interferences (see Figure 3.1) at the interfaces between the various 2D layers [76]. Here we develop a quantitative model based on Fresnel's equations for the Raman Factor F_{2DM} and exclusive light absorption in a 2DM A_{2DM}.
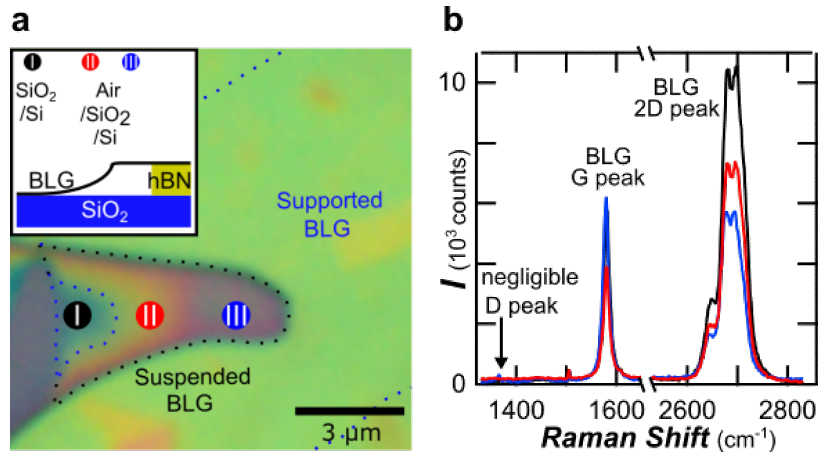
Figure 3.1: Interference in BLG heterostructure. (a) Optical image of device BB1 with three distinct regions labeled I, II and III. Inset: diagram of the heterostructure geometry. (b) Raman spectra acquired at the numbered circles location in the optical picture.

3.1.1 Exclusive Light Absorption

Our heterostructures function as optical cavities with multiple layers, and have dimensions comparable to the incident light wavelength ($\lambda = 532$ nm). Interference effects must be included as these greatly impact the graphene light absorption A_{Gr}, reflection R_{Gr} and transmission T_{Gr}. Our simple theoretical models are based on Fresnel's equations (derivation in appendix)[69]. The exclusive light absorption model predicts an absorption of about 2.3% for a SLG (4.6% BLG) surrounded by vacuum in the EM visible range, this is what the theory based on solid state concepts predicts as well as the experimental results [45].

$$A_{\mathrm{Gr}} = 1 - R_{\mathrm{Gr}} - T_{\mathrm{Gr}} \tag{3.1}$$

When light strikes the interface between a medium with refractive index n_1 and a second medium with refractive index n_2, both reflection and refraction of the light may occur (Fig. 3.2). The Fresnel equations describe the ratios of the reflected and transmitted electric fields to the incident electric field (the wave magnetic fields can also be related using similar coefficients). Since these are complex ratios, they describe not only the relative amplitude, but phase shifts between the waves. The equations assume the interface between the media is flat and that the media are homogeneous and isotropic. The incident light is assumed to be a plane wave, which is sufficient to solve any problem since any incident light field can be decomposed into plane waves and polarizations. Fresnel's coefficients for reflection and transmission are $r_{i,j}$ and $t_{i,j}$, the subscripts are numerical and represent the two media at the interface. At normal light incidence and for both p- (E-field parallel to the incident plane) and s-polarized (E-field perpendicular to the incident plane) light we have [69],

$$\tilde{r}_{\mathrm{i,j}} = \frac{\tilde{n}_{\mathrm{i}} - \tilde{n}_{\mathrm{j}}}{\tilde{n}_{\mathrm{i}} + \tilde{n}_{\mathrm{j}}} \tag{3.2}$$

$$\tilde{t}_{\mathrm{i,j}} = \frac{2\tilde{n}_{\mathrm{i}}}{\tilde{n}_{\mathrm{i}} + \tilde{n}_{\mathrm{j}}} \tag{3.3}$$

The phase shift encountered at the interface is defined as,

$$\tilde{\beta}_i = k\tilde{n}_i h_i = \frac{2\pi}{\lambda}\tilde{n}_i h_i \tag{3.4}$$

Where, $\tilde{n}_i$ is the complex index of refraction of medium i h_i is the medium thickness and λ is the incident wavelength. As seen before in chapter 1, the total absorption is,

$$A_{2DM} = 1 - R_{2DM} - T_{2DM} \tag{3.5}$$

Total reflection and transmission are defined in terms of the incident, reflected and transmitted power P as follows,

$$R = \frac{P_r}{P_i} = \left(\frac{\vec{E}_r}{\vec{E}_i}\right)^2 = |\tilde{r}|^2 \tag{3.6}$$

$$T = \frac{P_t}{P_i} = \frac{\tilde{n}_t}{\tilde{n}_i}\left(\frac{\vec{E}_t}{\vec{E}_i}\right)^2 = \frac{\tilde{n}_t}{\tilde{n}_i}|\tilde{t}|^2 \tag{3.7}$$
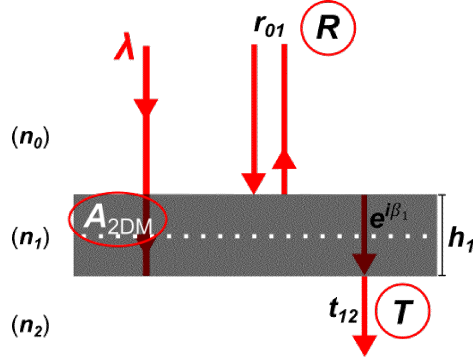
Figure 3.2: Important parameters in a 3 media system. Incident light of wavelength λ is transmitted T, reflected R and absorbed A_{2DM}. The terms $\tilde{r}_{01}$ and $\tilde{t}_{12}$ are the reflection (from first interface) and transmission (second interface) coefficients. $e^{i\tilde{\beta}_1}$ is the propagator inside medium 1 and h_1 is its thickness.

All indices of refraction depended on the incident light wavelength. The coefficients for a three media system are,

$$\tilde{r}_{3 \text{ media}} = \frac{\tilde{r}_{01} + \tilde{r}_{12}e^{2i\tilde{\beta}_1}}{1 + \tilde{r}_{01}\tilde{r}_{12}e^{2i\tilde{\beta}_1}} \tag{3.8}$$

$$\tilde{t}_{3 \text{ media}} = \frac{\tilde{t}_{01}\tilde{t}_{12}e^{i\tilde{\beta}_1}}{1 + \tilde{r}_{01}\tilde{r}_{12}e^{2i\tilde{\beta}_1}} \tag{3.9}$$

We use a recursive method to obtain these coefficients, and therefore, the exclusive absorption for any number of media [19].

$$\tilde{r}_{\text{N media}} = \frac{\tilde{r}_{01} + \tilde{r}_{\text{N-1 media}}e^{2i\tilde{\beta}_1}}{1 + \tilde{r}_{01}\tilde{r}_{\text{N-1 media}}e^{2i\tilde{\beta}_1}} \tag{3.10}$$

$$\tilde{t}_{\text{N media}} = \frac{\tilde{t}_{01}\tilde{t}_{12}e^{i\tilde{\beta}_1}}{1 + \tilde{r}_{01}\tilde{r}_{\text{N-1 media}}e^{2i\tilde{\beta}_1}} \tag{3.11}$$

Where, $\tilde{r}_{\text{N media}}$ and $\tilde{t}_{\text{N media}}$ depend on the coefficients $\tilde{r}_{\text{N-1 media}}$ and $\tilde{t}_{\text{N-1 media}}$ in a recursive way. In order to get the coefficients for a four media system, we simply plug the coefficients for a three media system (equations 3.8 and 3.9) into equations 3.10 and 3.11 respectively. We get,

$$\tilde{r}_{4 \text{ media}} = \frac{\tilde{r}_{01} + \tilde{r}_{12}e^{2i\tilde{\beta}_1} + [\tilde{r}_{01}\tilde{r}_{12}e^{2i\tilde{\beta}_1}]\tilde{r}_{23}e^{2i\tilde{\beta}_2}}{1 + \tilde{r}_{01}\tilde{r}_{12}e^{2i\tilde{\beta}_1} + [\tilde{r}_{01}\tilde{r}_{12}e^{2i\tilde{\beta}_1}]\tilde{r}_{23}e^{2i\tilde{\beta}_2}} \tag{3.12}$$

$$\tilde{t}_{4 \text{ media}} = \frac{\tilde{t}_{01}\tilde{t}_{12}\tilde{t}_{23}e^{i(\tilde{\beta}_1+\tilde{\beta}_2)}}{1 + \tilde{r}_{01}\tilde{r}_{12}e^{2i\tilde{\beta}_1} + [\tilde{r}_{01}\tilde{r}_{12}e^{2i\tilde{\beta}_1}]\tilde{r}_{23}e^{2i\tilde{\beta}_2}} \tag{3.13}$$
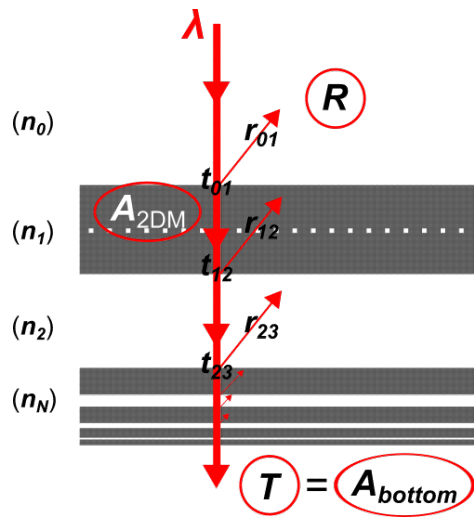
Figure 3.3: Parameters in a multimedia system. Absorption occurs first in medium 1, reflection occurs at each interface and the overall transmission is equal to the absorption by the bottom media. No light can transmit in metallic bottom.

3.1.2 Raman factor

Our light absorption measurements are perform using Raman spectroscopy. Our interest is the exclusive absorption of graphene, where in addition to the interference due to multiple reflection of the incident light, the multiple reflection of the Raman scattered light (Raman signal) has to be considered (Fig. 3.4) [70, 72, 71]. The total enhancement factor of the measured Raman signal (Raman factor) is calculated by the equation [66],
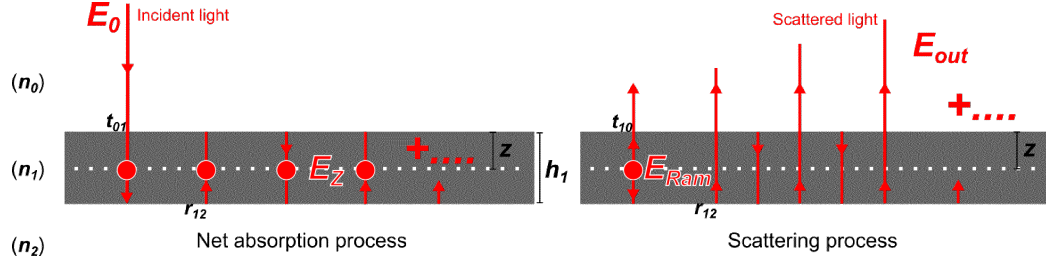
Figure 3.4: Schematic illustration of multiple reflection interference. E_0 is the incident E-field, E_z is the E-field inside medium 1. E_{Ram} is the Raman scattered E-field produced inside medium 1, this goes through multiple reflections before going out as E_{out}.

$$F_{\mathrm{Gr}} = N \int_0^{h_{\mathrm{Gr}}} |F_{\mathrm{ab}} \cdot F_{\mathrm{sc}}|^2 \, dz \tag{3.14}$$

Where, the first term $F_{\mathrm{ab}} = \vec{E}_z / \vec{E}_0$ is related to the net absorption, the second $F_{\mathrm{sc}} = \vec{E}_{out} / \vec{E}_{Ram}$ to the scattering processes (Fig. 3.4) and N is the normalization constant. This constant is found for the case of free-standing graphene surrounded by vacuum, it is the reciprocal number of the intrinsic Raman intensity when no interference effects are present. The measured Raman scattering intensity I is $I = I_{\mathrm{i}} \cdot F_{\mathrm{Gr}}$, where I_{i} is the intrinsic Raman intensity [66, 70]. The two optical processes in a 3 media system are described by,

$$F_{\mathrm{ab, \, 3media}} = \tilde{t}_{01} \frac{e^{-i\tilde{\beta}_z} + \tilde{r}_{12} e^{-i(2\tilde{\beta}_1 - \tilde{\beta}_z)}}{1 + \tilde{r}_{12}\tilde{r}_{10} e^{-2i\tilde{\beta}_1}} \tag{3.15}$$

$$F_{\mathrm{sc, \, 3media}} = \tilde{t}_{10} \frac{e^{-i\tilde{\beta}_z} + \tilde{r}_{12} e^{-i(2\tilde{\beta}_1 - \tilde{\beta}_z)}}{1 + \tilde{r}_{12}\tilde{r}_{01} e^{-2i\tilde{\beta}_1}} \tag{3.16}$$

Where, $\tilde{\beta}_z$ is the phase shift introduced in the graphene layer where the Raman interaction occurs. Equation 3.14 can also be extended to any number of media by a similar recursive method,

$$F_{\text{ab, Nmedia}} = \tilde{t}_{01} \frac{e^{-i\tilde{\beta}_z} + \tilde{r}_{\text{N-1 media}} e^{-i(2\tilde{\beta}_1 - \tilde{\beta}_z)}}{1 + \tilde{r}_{\text{N-1 media}} \tilde{r}_{01} e^{-2i\tilde{\beta}_1}} \tag{3.17}$$

$$F_{\text{sc, Nmedia}} = \tilde{t}_{10} \frac{e^{-i\tilde{\beta}_z} + \tilde{r}_{\text{N-1 media}} e^{-i(2\tilde{\beta}_1 - \tilde{\beta}_z)}}{1 + \tilde{r}_{\text{N-1 media}} \tilde{r}_{01} e^{-2i\tilde{\beta}_1}} \tag{3.18}$$

The equations for 4 media are obtained by plugging equations 3.15 and 3.16 into 3.17 and 3.18 respectively,

$$F_{\text{ab, 4media}} = \tilde{t}_{01} \frac{[1 + \tilde{r}_{12}\tilde{r}_{23}e^{-i\tilde{\beta}_2}]e^{-i\tilde{\beta}_z} + [\tilde{r}_{12} + \tilde{r}_{23}e^{-i\tilde{\beta}_2}]e^{-i(2\tilde{\beta}_1 - \tilde{\beta}_z)}}{1 + \tilde{r}_{12}\tilde{r}_{23}e^{-i\tilde{\beta}_2} + [\tilde{r}_{12} + \tilde{r}_{23}e^{-i\tilde{\beta}_2}]\tilde{r}_{01}e^{-2i\tilde{\beta}_1}} \tag{3.19}$$

$$F_{\text{sc, 4media}} = \tilde{t}_{10} \frac{[1 + \tilde{r}_{12}\tilde{r}_{23}e^{-i\tilde{\beta}_2}]e^{-i\tilde{\beta}_z} + [\tilde{r}_{12} + \tilde{r}_{23}e^{-i\tilde{\beta}_2}]e^{-i(2\tilde{\beta}_1 - \tilde{\beta}_z)}}{1 + \tilde{r}_{12}\tilde{r}_{23}e^{-i\tilde{\beta}_2} + [\tilde{r}_{12} + \tilde{r}_{23}e^{-i\tilde{\beta}_2}]\tilde{r}_{01}e^{-2i\tilde{\beta}_1}} \tag{3.20}$$

The incident wavelength is used in the net absorption term and the G (2D) related wavelength is used in the scattering term. The incident light has a wavelength of 532 nm and is scattered, giving rise to the two prominent G and 2D peaks in the graphene spectrum (Fig. 3.1). The wavelength related to the G peak is 581 nm (1580 cm^{-1}) and for 2D (2700 cm^{-1}) peak is 621 nm. It is calculated by [72],

$$\omega_{\text{Ram}}(\text{cm}^{-1}) = \left| \frac{1}{\lambda_0(\text{nm})} - \frac{1}{\lambda_{\text{sc}}(\text{nm})} \right| * 10^7 \tag{3.21}$$

Where, ω_{Ram} is the Raman shift. We now plot the Raman factor F_{BLG} and

exclusive light absorption A_{BLG} for air/BLG/SiO$_2$/Si (4 media) as a function of SiO$_2$-spacer thickness.
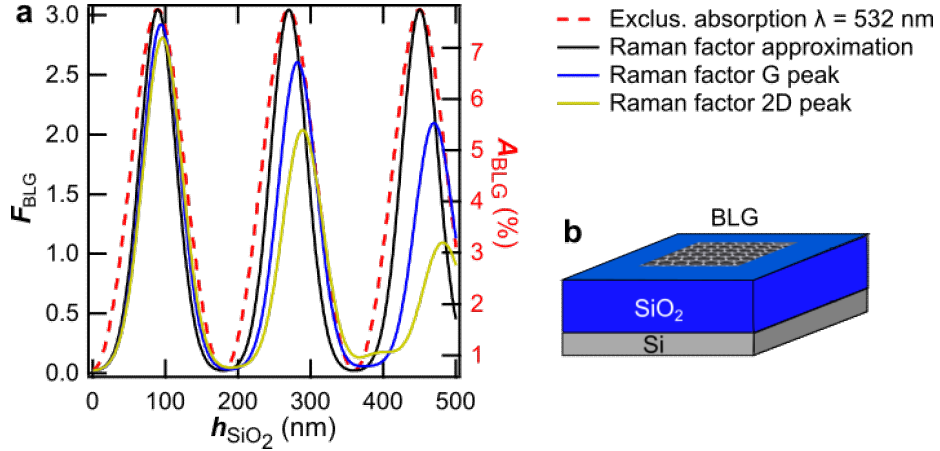
Figure 3.5: Calculated Raman factor and exclusive light absorption for BLG on SiO$_2$-spacer as a function of spacer thickness. (a) Plot of BLG Raman factor (left axis) and exclusive light absorption (right axis) as a function of SiO$_2$ thickness. (b) Illustration of BLG heterostructure.

Figure 3.5 is the calculated Raman factor enhancement relative to the free-standing BLG case (solid lines) and the exclusive light absorption (dashed line). The solid black curve was obtained in a simple approximation where the Raman bands (G and 2D) and the incident light are taken to have the same wavelength, blue corresponds to the G and gold to the 2D related wavelength. Our samples are made of 310 nm of SiO$_2$ (measured by reflectometry) and we get a Raman factor of 1.48 and 1.53 for the G and 2D peaks respectively, which correspond to an exclusive light absorption of 4.25%. These Raman factors are directly related to the integrated Raman intensity, the area under the G and 2D peak (derivation of both theoretical models in appendix).

3.1.3 Fit of G and 2D Peaks to Get Integrated Raman Intensity

The calculated Raman factor for the G and 2D peaks correspond to their integrated Raman intensity, the area under the curves. In order to extract this number, we perform a fit of the experimental curves using a single Lorentzian (G) and a combination of four Lorentzian functions (2D). In figure 3.6 we show the raw data,

fit curves and extracted integrated Raman intensity.
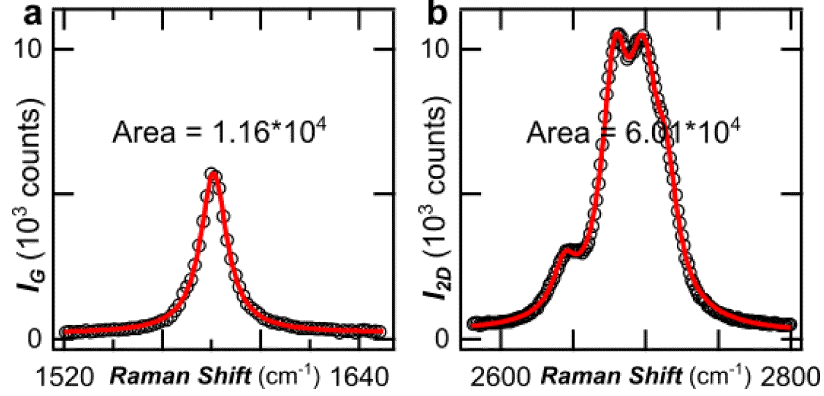
Figure 3.6: Curve fit to extract the integrated Raman intensity of BLG on 310 nm of SiO$_2$. Open black circles are raw data and red curve is the fit for (a) G and (b) 2D peak.

The G peak is fit using a single Lorentzian function of the form:

$$f(x) = y_0 + m(x - x_0) + \left(\frac{2A}{\pi}\right)\left(\frac{FWHM}{4(x - x_0)^2 + FWHM^2}\right) \qquad (3.22)$$

where, y_0 is the offset, x_0 is the G peak position, A is the amplitude, $FWHM$ is the full-wave-half-maximum and m is the slope of the curve.

The 2D peak is fit using a combination of four Lorentzian functions of the form:

$$f(x) = y_0 + m(x - x_0) + \left(\frac{2A}{\pi}\right)a + \left(\frac{2B}{\pi}\right)b + \left(\frac{2C}{\pi}\right)c + \left(\frac{2D}{\pi}\right)d \qquad (3.23)$$

With coefficients $a = \frac{FWHM_a}{4(x-x_a)^2+FWHM_a^2}$, $b = \frac{FWHM_b}{4(x-x_b)^2+FWHM_b^2}$, $c = \frac{FWHM_c}{4(x-x_c)^2+FWHM_c^2}$ and $d = \frac{FWHM_d}{4(x-x_d)^2+FWHM_d^2}$. Where, y_0 is the offset, x_0 is the 2D peak position, A is the amplitude of first, B second, C third, D forth Lorentzian, $FWHM_{a,b,c,d}$ is the full-wave-half-maximum and $x_{a,b,c,d}$ is the position of the respective function, and m is the slope of the curve. We finally remove the background offset and slope, i.e. set y_0 and m equal to zero. This eliminates the background (not graphene) signal, as we integrate over the range shown in Figure 3.6. Changing the range of integration does not change the extracted number of counts (Raman intensity).

3.2 Instrumentation and Calibration

For optical measurements, we use a Renishaw inVia Raman spectrometer equipped with a Prior ProScan morotized translation stage (Fig. 3.7), an Innovative Photonic Solutions 532 nm spectrum stabilized laser source (model I0532SR0050B), and a Leica DM LM optical microscope. According to specification, the translation stage has a spatial precision of $\pm 0.05 \mu$m for in-plane XY directions. Our laser spot has a Gaussian distribution when focused onto the sample, and its width depends on the objective used. For our 50x and 100x objectives, our spot is elliptical with FWHM between 336 nm and 432 nm. Renishaw's WiRE software controls the translation stage and has many customizable acquisition options, including acquisition time laser power, mapping dimensions, automatic laser focusing, and more. The holographic filters fulfill the same function as a dichroic mirror, directing the excitation laser beam toward the sample, and allowing the scattered light to pass through it toward the diffraction grating and CCD camera (figure 3.8) [86].
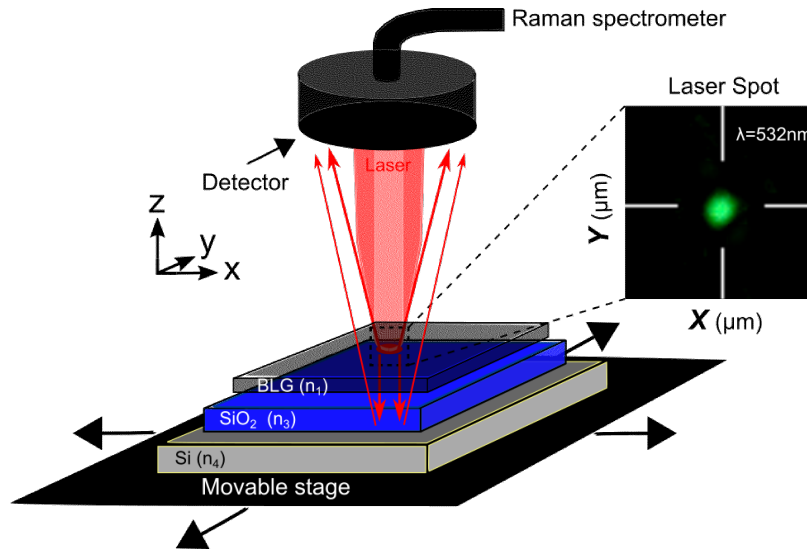
Figure 3.7: Raman spectrometer apparatus. A laser with wavelength 532 nm is normally incident on our sample held on a motorized stage. Raman scattered light is collected by the detector around the objective. Inset: Optical image of the laser spot.

50

3.2.1 Laser beam characterization

In order to characterize our laser spot, we focus the laser on the Si substrate with a 100x microscope objective (NA = 0.80), adjust the camera acquisition time such that the laser spot is clearly visible and not saturated, and then capture the image. Next, we convert the image to grayscale, where the value of each pixel becomes a measure of intensity. Once we plot the data in Igor Pro 7, we can then fit the intensity profile with the 2D Gaussian function:

$$f(x, y) = A exp(-(a(x - x_0)^2 + 2b(x - x_0)(y - y_0) + c(y - y_0)^2)) \qquad (3.24)$$

with coefficients $a = \frac{cos^2(\theta)}{2\sigma_x^2} + \frac{sin^2(\theta)}{2\sigma_y^2}$, $b = -\frac{sin^2(2\theta)}{4\sigma_x^2} + \frac{sin^2(2\theta)}{4\sigma_y^2}$, $c = \frac{sin^2(\theta)}{2\sigma_x^2} + \frac{cos^2(\theta)}{2\sigma_y^2}$, where A is the amplitude, $\sigma_{x,y}$ are the widths along the x and y axes, and θ is the rotation of the Gaussian spot. From this fit we can extract the FWHM for each axis according to:

$$FWHM_{x,y} = 2\sqrt{2ln(2)\sigma_{x,y}} \qquad (3.25)$$

The raw data and resulting fit are shown in figure 3.12, displaying our elliptical spot. From the narrow and wide cross-sections, we extract $FWHM_x = 336nm$ and $FWHM_y = 432nm$, as shown in figure 4.2 [86].
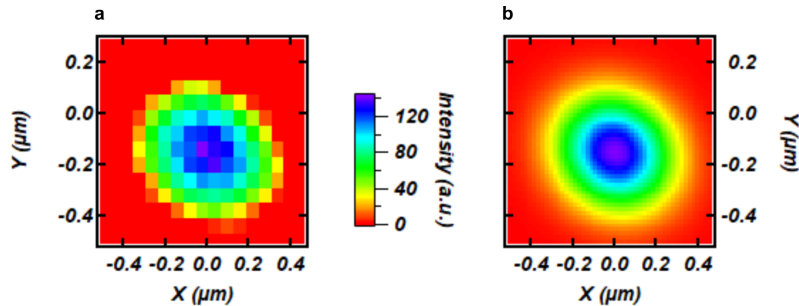
Figure 3.8: Laser spot characterization via Gaussian fit. (a) Shows an image of measured laser spot intensity reflected from the Si/SiO2 substrate through a 100x microscope objective. (b) Shows a 2D gaussian fit of the laser spot image. Our spot appears to be elliptical with an approximated size of 0.8 um. Figure reproduced from [86].

3.2.2 Raman Intensity Focus Test

Figure 3.9 shows Raman measurements on a large area BLG crystal. This crystal is used to calibrate Raman intensity as a function of laser focus position. Figure 3.9a shows the position of a Raman scan on the calibration crystal. This Raman scan is repeated for three different z-axis positions with respect to the BLG surface. Figure 3.9b schematically illustrates the focus position (z-axis), I is right on the crystal's surface (0 nm), II focused 150 nm above it, and III focused 300 nm above it. Figure 3.9c shows that the Raman intensity of the G peak. Black curves were taken at position I, red ones at position II, and blue ones at III. Top view optical images of the laser spot are found as insets. Figure 3.9d shows the 2D peak. All intensities unaltered for this focus position range. This suggests that laser beam cross-sectional area is the important parameter for Raman intensity in this range.
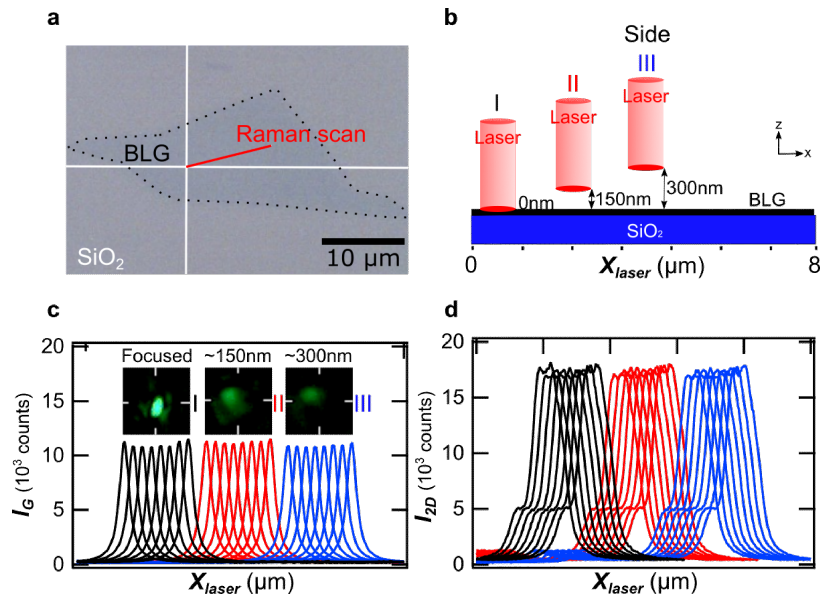
Figure 3.9: Focus test on calibration BLG crystal. (a) Optical image of the BLG with Raman line scan in red. (b) Schematic illustration of the focal point position (z-axis) for three different positions on and above the BLG surface. (c) Raman scattering intensity of the G peak for the focal point positions in (b). Insets: Optical images of laser spot. (d) Raman scattering intensity of the 2D peak. Intensity remains the same in the three cases.

52

3.2.3 Reproducibility of Raman Intensity Measurements

Figure 3.10: Raman intensity of tilted device BB1 in day 1. (a) Top view optical image of device BB1 with 4 distinct regions labelled I, II, III and IV. Inset: Cross-sectional diagram. (b),(c) Raw Raman intensity as a function of laser position for G and 2D peak respectively. (d),(e) Integrated Raman intensity as a function of laser position for G and 2D peak respectively.

Figure 3.10 shows performed Raman intensity measurements as a function of laser position in device BB1 (hybrid geometry). This tilted BLG/air(varying)/SiO$_2$ NOEMS with variable air-spacer thickness is a highly dynamic system. As mentioned in Chapter 2, there are dynamic interactions of the BLG crystal and its underlying SiO$_2$ substrate until it reaches a configuration as that of Figure 3.11a. This device has four well defined regions: BLG supported on a 310 nm SiO$_2$-spacer/silicon substrate in region I (black circle), suspended BLG on air-spacer of varying thickness in region II (red), suspended BLG on air-spacer of fairly constant thickness in region III (blue), and BLG supported on a hBN-spacer with 160 nm thickness in region IV (gold). Figure 3.10a, shows a top view image of device BB1 (inset is a side view cartoon) with the Raman scan position in dashed red line. In Figures 3.10b,c, shows a plot of raw Raman scattering intensity as a function of laser position x_{laser}

for both G and 2D peaks respectively. In Figures 3.10d,e, we show the plot of the integrated Raman intensity (extracted as explained in Section 3.1.3) as a function of laser position for both peaks. Region II shows strong destructive/constructive interference, caused by the varying air-spacer thickness. This effect on the Raman factor will be modelled next.
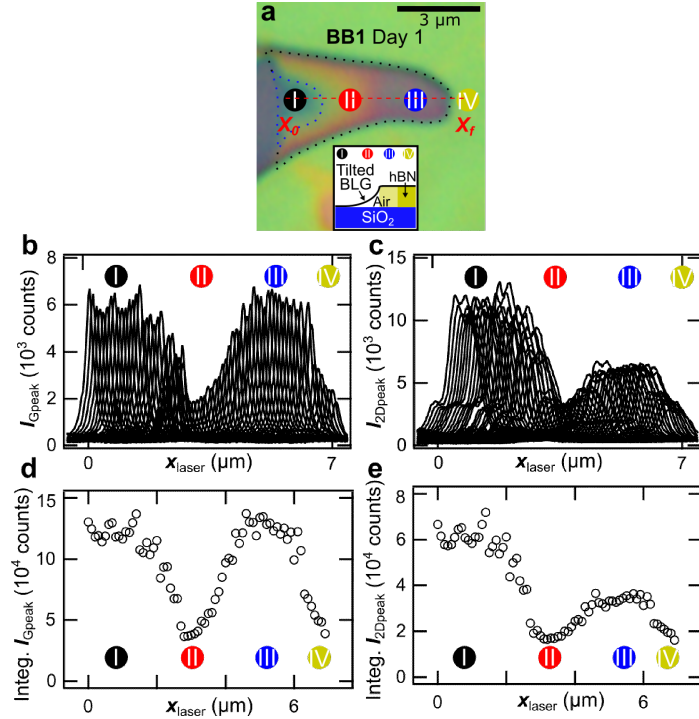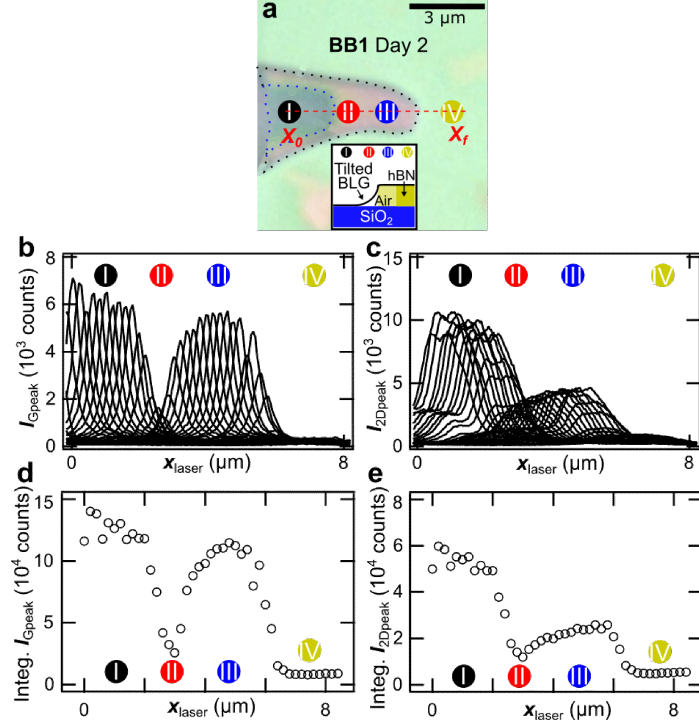

Figure 3.11: Raman intensity of tilted device BB1 in day 2. (a) Top view optical image of device BB1 with 4 distinct regions labelled I, II, III and IV. Inset: Cross-sectional diagram. (b),(c) Raw Raman intensity as a function of laser position for G and 2D peak respectively. (d),(e) Integrated Raman intensity as a function of laser position for G and 2D peak respectively.

In Figure 3.11, we show the same tilted NOEMS a day later. In Figure 3.11a we can clearly see how region I covers a greater area. This is the final configuration of the device (up to months after fabrication) when it has reached an equilibrium position. Region II has decreased in size, meaning a faster ramp up between the BLG completely in contact with SiO_2 and suspended at 160 nm above it. Region III remains almost the same as well as region IV. In Figures 3.11b,c, we plot the raw Raman scattering intensity as a function of laser position for both G and 2D peaks respectively. In Figures 3.11d,e, we show the plot of the integrated Raman intensity

as a function of laser position for both peaks. We repeat this Raman measurement several times after(day 3, 30, 80), obtaining the same results. This indicates a robust Raman measurement process that is reproducible.

3.2.4 Proportionality between measured Raman intensity and Raman factor

To establish the proportionality between the measured Raman intensity and the theoretical Raman factor, we use a single heterostructure geometry (air/BLG/310nm-SiO_2/Si) as the one in region I of Figure 3.1. We previously calculated a theoretical Raman factor of 1.48 and 1.53 for the G and 2D peak respectively for such geometry (Section 3.1.2). In Figure 3.12 we show five such heterostructures with exfoliated BLG (pristine), Raman data was aquired along the red lines. In Figure 3.12a, a calibration device is shown. In Figures 3.12b-e, the BLG crystals (before stamping) for devices BA1-4 are shown. Figures 3.12f,g are plots of the ratio between Raman intensity and laser power per unit area (μm^2) for the G and 2D peaks respectively. We find a proportionality constant of 5.6 counts*$\mu m^2/\mu W$*s for a theoretical Raman factor of 1.48 (G) and 19.2 counts*$\mu m^2/\mu W$*s for a factor of 1.53 (2D). This is then used to compare to other heterostructure geometries, such as the on-substrate devices BA1-4 (air/BLG/hBN/Al), tilted BB1 and suspended devices (air/BLG/air/310nm-SiO_2/Si). This proportionality applies to our instrumentation parameters (reflection mode spectrometer, laser power per unit area, laser spot size) as described in previous sections.
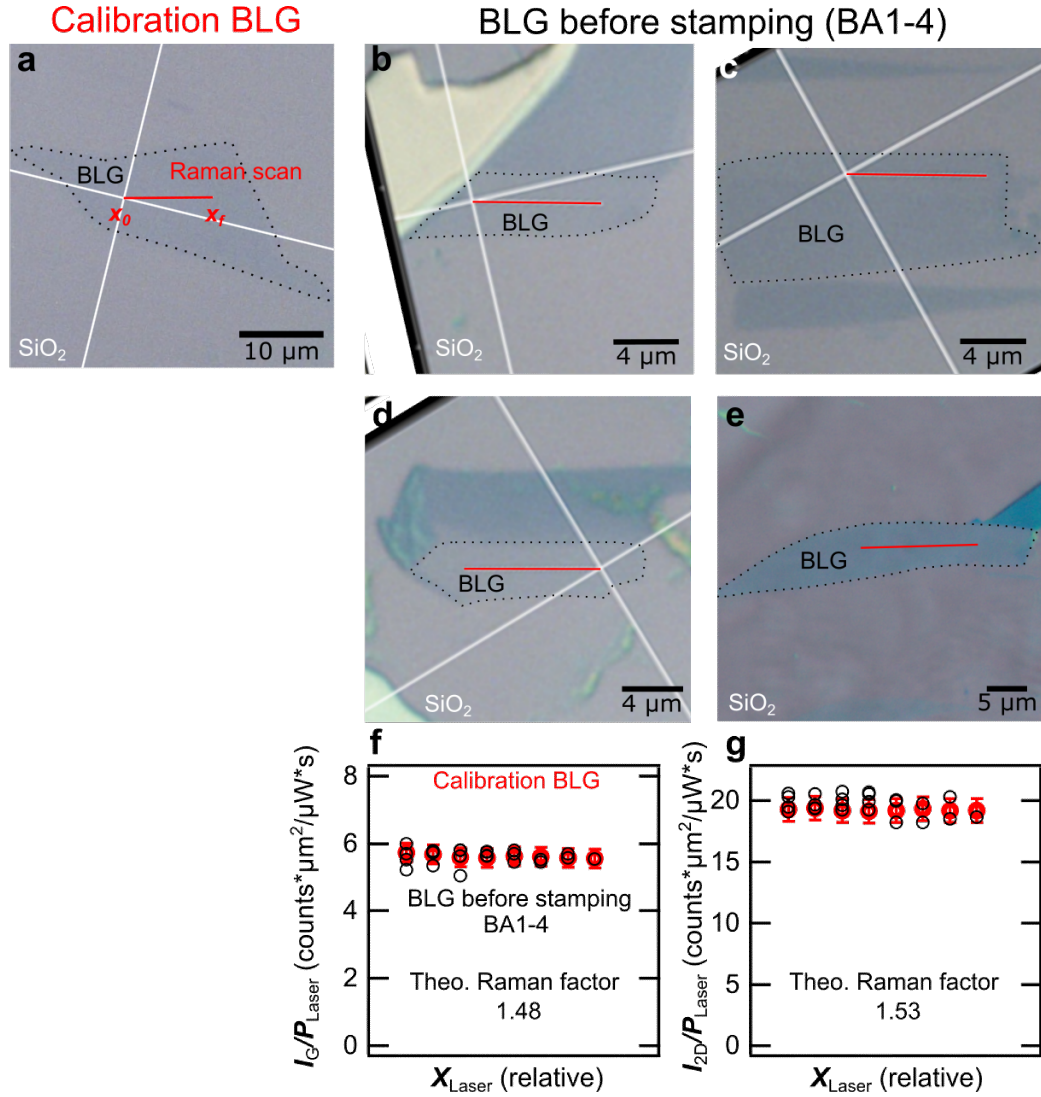
Figure 3.12: Raman intensity calibration for BLG on 310 nm of SiO$_2$. (a) Top view optical image of a calibration BLG crystal and (b)-(e) four BLG crystals before stamping. (f),(g) Plot of the ratio between Raman scattering intensity and laser power per unit area for both G and 2D peaks respectively. Raman data for the calibration BLG is in red open circles and all others in black ones.

3.3 Tunable Light Absorption in Stamped 2D NOEMS

Figure 3.13a is a top view of one of four BLG/hBN/Al heterostructures with various hBN spacer thicknesses ($370, 385, 435, 445 \pm 10$ nm). The red dashed line shows the location of the AFM measurement of the hBN thickness displayed at the bottom left of the panel. Figure 3.13b-c show the measured G and 2D Raman factor (circles) on each of the 4 BLG/hBN/Al heterostructures and the theoretical model (solid curve). There is a strong quantitative agreement, and the measured tunability of the Raman factor for the G-peak is up to 19 folds. This would permit to strongly enhance the weak Raman signals predicted in many-body phase transitions [51] without requiring a disruptive increase in laser power. The corresponding underlying exclusive light absorption in the theoretical model is shown in the inset of Figure 3.13c. Figure 3.13c shows a top view of tilted-suspended BLG/air(variable thickness)/SiO$_2$ heterostructure (see the inset and Figure 3.10c for side-view diagram). The labels I, II, III correspond to the regions where the air-spacer thickness is respectively 0 nm, variable from 0 to 160 nm, and 160 nm thick. Such a structure is an ideal platform to quantitatively demonstrate the tuning of interferences which enhance or reduce Raman scattering in the BLG (Raman factor), and the underlying exclusive light absorption, in BLG as a function of the air-spacer thickness. Figure 3.13e-f show the Raman factor data (circles) for the G-peak and 2D-peak measured on the BLG heterostructure in Figure 3.13c. A Raman factor of 1 correspond to the Raman scattering intensity for an isolated BLG in vacuum, and was carefully calibrated as described in the Sections 3.1 and 3.2. The solid trace is a first-principle calculation (equation 3.14, F_{Gr}) with no fit parameter based on Fresnel's equations and the frequency dependent index of refractions of the media in the heterostructure. We find robust quantitative agreement between the data and model for both the G and 2D Raman modes. This strongly support that the underlying exclusive light absorption, stemming from the same model, of BLG at the 532-nm laser wavelength is modulated from less than 2% to almost 10% as shown in the inset of Figure 3.13f.
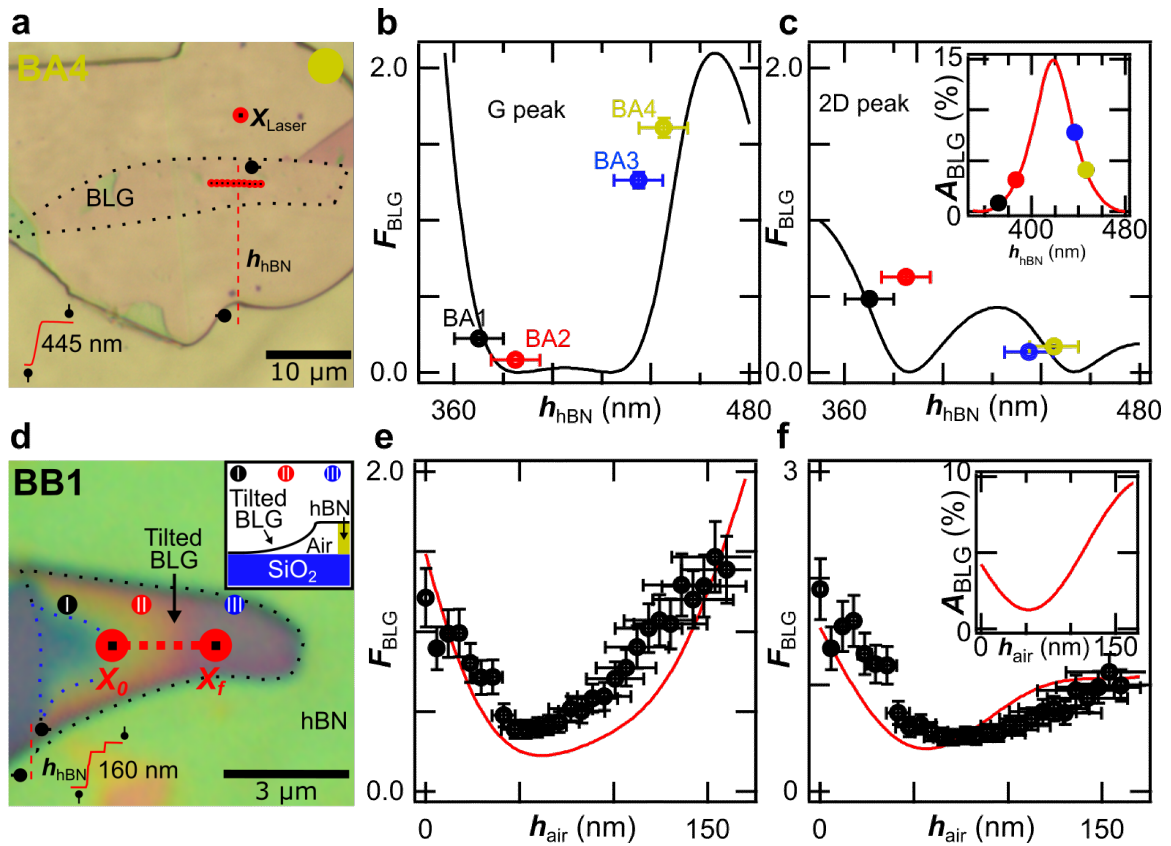
Figure 3.13: Tunable light absorption in stamped BLG heterostructures. (a) Top view optical image of stamped BA4 device with position of Raman measurements in red markers. Bottom left, AFM trace indicating a hBN-spacer thickness of 445 nm. (b) Experimental (coloured circles) and theoretical (solid line) Raman factor of devices BA1-4, as a function of hBN-spacer thickness for the G and (c) 2D peak. Inset: BLG exclusive absorption as a function of hBN-spacer thickness. (d) Top view optical image of tilted device BB1 with location of Raman measurement in red dashed line and tree distinc regions labelled I, II and III. Bottom left, AFM trace indicating a hBN-trench thickness of 160 nm. Inset: Cross-sectional diagram. (e) Experimental (open circles) and theoretical (solid line) Raman factor as a function of air-spacer varying thickness for the G and (f) 2D peak. Inset: BLG exclusive absorption as a function of air-spacer varying thickness.

58

Figure 3.14a is a top view of one of three suspended $Gr/air/SiO_2$ heterostructures (1 SLG and 2 BLG) with various air spacer thicknesses ($460,1150,1340 \pm 25$ nm). The red dashed line shows the location of the AFM measurement of the air thickness displayed at the bottom left of the panel. Figure 3.14b-c show the measured G and 2D Raman factor (circles) on each of the 3 $BLG/air/SiO_2$ heterostructures and the theoretical model (solid curve). The quantitative agreement between the measurement and model confirms that it will be possible to enhance both the Raman factor and light absorption in transferred suspended SLG and BLG heterostructures. Simple lithographic deposition of a bottom gate electrode and top electrical contacts before the stamping of BLG, should permit to gate-control the thickness of the air space over a 100 nm range and lead to order of magnitude in-situ tunability of light absorption in BLG and other 2DMs.
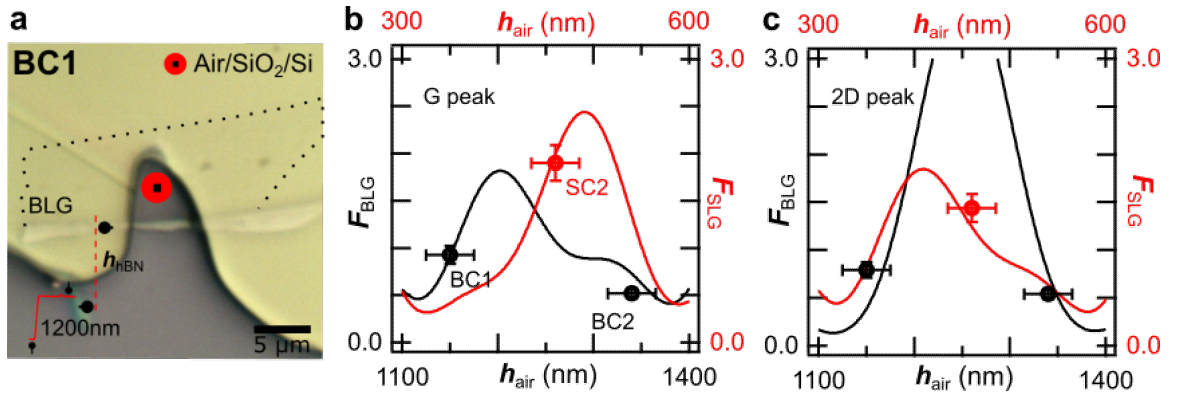
Figure 3.14: Tunable light absorption in suspended graphene NOEMS. (a) Top view optical image of suspende device BC1 with location of Raman measurement (red marker). Bottom left, AFM trace indicating a hBN-trench thickness of 1150 nm. (b) Experimental (coloured circles) and theoretical (solid line) Raman factor of devices BC1-2 (left and bottom axes), SC2 (in red, right and top axes) as a function of crystal suspension height for the G and (c) 2D peak.

The overall uncertainty in our measured Raman factor is calculated using standard error propagation analysis [39]. It includes uncertainty due to fluctuations (noise) of the Raman scattering intensity ΔI and the fit of G and 2D peak ΔI_{fit}.

$$\frac{\Delta Raman\,factor}{Raman\,factor} = \sqrt{\left(\frac{\Delta I}{I}\right)^2 + \left(\frac{\Delta I_{\text{fit}}}{I_{\text{fit}}}\right)^2} \tag{3.26}$$

Table 3.1 summarizes all wavelength dependent indices of refraction [81, 82, 83, 84, 85].

Material	Real part of $\tilde{n}$	Imaginary part of part of $\tilde{n}$
BLG (532nm)	2.33	1.3
BLG (581nm)	2.41	1.373
BLG (621nm)	2.47	1.43
Al (532nm)	0.636	5.38
Al (581nm)	0.794	5.88
Al (621nm)	0.948	6.26
SiO$_2$ (532nm)	1.475	-
SiO$_2$ (581nm)	1.473	-
SiO$_2$ (621nm)	1.47	-
Si (532nm)	4.14	0.033
Si (581nm)	3.98	0.22
Si (621nm)	3.89	0.017

Table 3.1: List of complex indices of refraction for different material and wavelength

Among all materials only hBN has an analytical equation for its index of refraction of the form [82, 83],

$$n_{\text{hBN}}(\lambda) = \sqrt{1 + \frac{3.263\lambda}{\lambda^2 - 164.4^2}} \qquad (3.27)$$

Chapter 4

Summary of Main Results and Outlook

This chapter summarizes the three main results of this thesis and provides an outlook.

4.1   Main Results

Firstly, our stamping method allows the direct pick-up of naked 2DMs exfoliated on SiO_2. This has the great advantage of having an easy and proven way to produce high quality, relatively large surface area 2D crystals by "Scotch tape" exfoliation [63]. We can completely characterize the 2DMs before and after the tranfer to test the quality of the fabrication process.

Secondly, it is the only existing stamping method to deterministically transfer suspended SLG and BLG over trenches (see Figure 4.1). As mentioned before, the fabrication of suspended 2DM-based devices was previously only possible through several complex steps in a clean room environment. This is a great achievement for the fast and reliable fabrication of large, suspended ultra-thin 2D crystal NOEMS.

Lastly, we show the ability to tune the Raman scattering intensity and the exclusive light absorption of BLG in three distinct device geometries (see Figure 4.2). The four stamped BLG optical cavities with hBN-spacer (different thickness) and aluminium reflector accomplished the greater on/off tunability, a factor of 19 for the Raman scattering and 18 for the light absorption. The detailed data set from our tilted BLG NOEMS device provided a quantitative agreement between the models
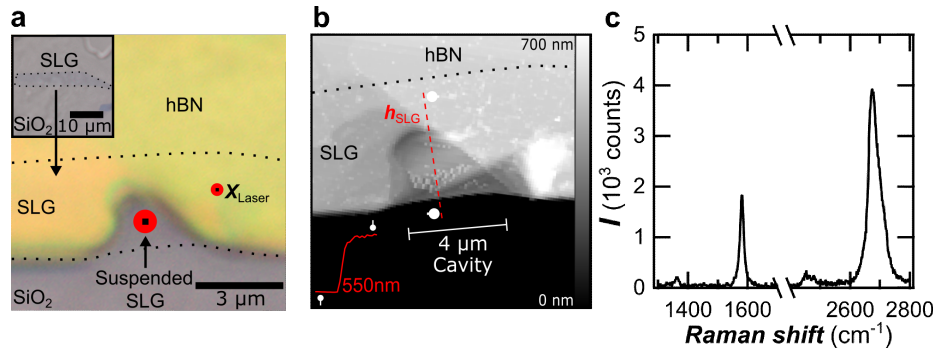
Figure 4.1: Suspended SLG heterostructure. (a) Optical image of suspended SLG with location of Raman laser (red dot). Inset: Optical image of SLG before transfer. (b) AFM image of device (a), the red dotted line is the position of the AFM trace indicating a crystal suspension of 550 nm. (c) Raman spectrum taken at position indicated in (a).

and measurements, as many data points were acquired along the air-spacer changing thickness. We showed that we can tune the graphene Raman scattering by 3.7 and light absorption by a similar amount in three suspended devices (two BLG and one SLG).
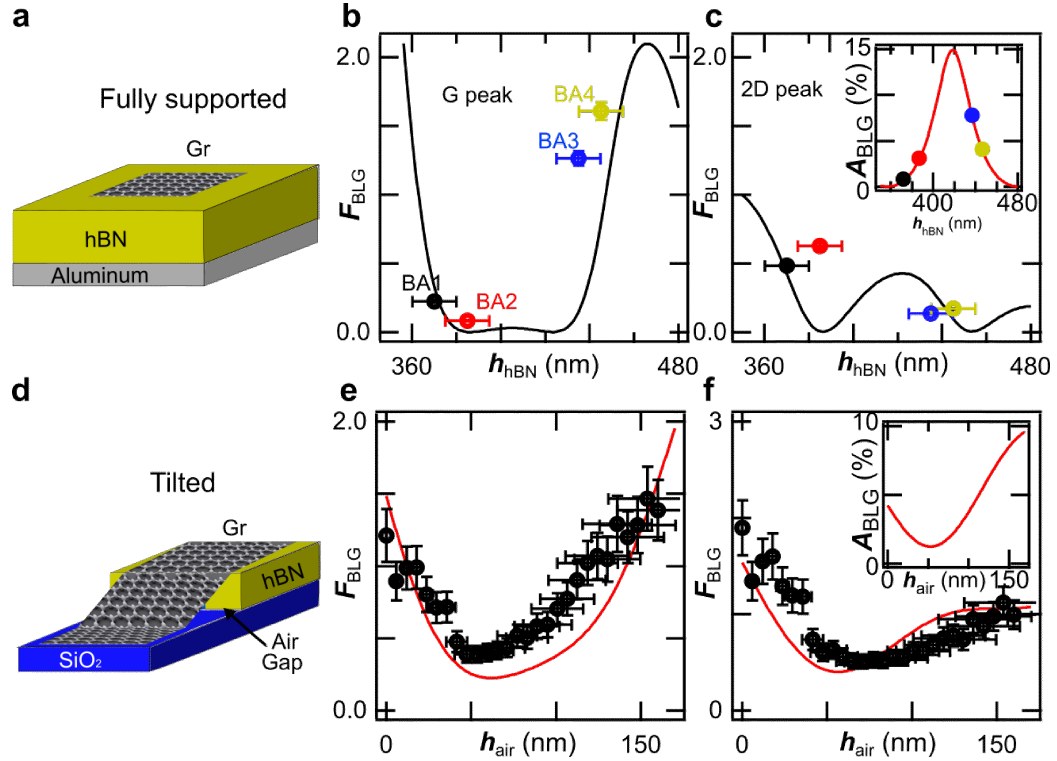
Figure 4.2: Tuning BLG Raman scattering intensity and light absorption in stamped BLG optical cavities. (a) Diagram of BLG/hBN/Aluminium devices. (b) Raman factor F_{BLG} of devices BA1-4 as a function of the hBN-spacer thickness for the G and (c) 2D peak. Inset: BLG exclusive light absorption A_{BLG} of devices in (b),(c). (d) Diagram of tilted BLG device. (e) Raman factor F_{BLG} of tilted device BB1 as a function of the air-spacer thickness for the G and (f) 2D peak. Inset: BLG exclusive light absorption A_{BLG} of devices BB1.

4.2   Outlook

The near future of this project is the fabrication of an optical transducer to achieve a high on/off ratio in terms of the BLG exclusive light absorption. In figure 4.3a, we can see a diagram of such a device, where the BLG suspended over an hBN trench and aluminium also has electrical contacts for transport. This allows for the BLG to be grounded and for a gate voltage to be applied, which deflects the crystal, essentially changing the suspension height, which determines the exclusive light absorption by interference effects. In Figure 4.3b, we show the optical image of our ingoing fabrication progress of such an optical transducer made with an hBN trench whose thickness is about 350 nm, an aluminium reflector at the bottom and an aluminium contact on top of the hBN trench. The trench length is about 3 μm and the contact is placed a couple of microns from the trench to allow the vdW interations between graphene and hBN to minimize slipping when deflected by the gate voltage. In Figure 4.3c, we modeled the BLG exclusive light absorption, using the theory presented in Chapter 3, as a function of the crystal suspension height. In a study by D. Metten [72], the relationship between the graphene deflection as a function of gate voltage for different trench lengths was reported. Given the dimensions of our structure, a gate voltage of about 20 Volts is sufficient to deflect the BLG by up to 100 nm and this will allows us to tune its light absorption from about 13% to 0%, in theory. The last steps remaining to complete the fabrication of this optical transducer are the stamping of BLG and wire bonding the contacts to a chip holder.
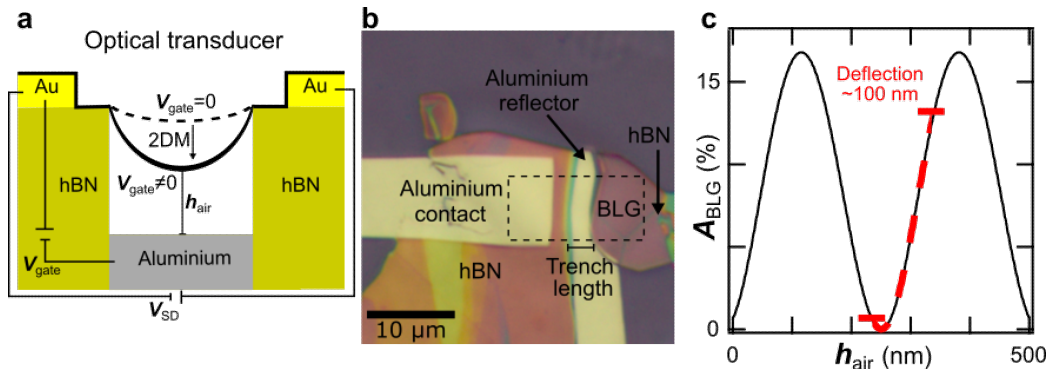
Figure 4.3: Optical transducer in progress. (a) Schematics of an optical transducer where a BLG is deflected by electrostatic means. (b) Optical image of our ongoing optical transducer. (c) Plot of BLG exclusive absorption as a function of crystal suspension.

There are several impactful applications that would benefit from the simpler assembly of devices using our fabrication method. A fundamental property of 2DMs that needs to be well-characterized is the thermal expansion coefficient. This parameter is instrumental to the fabrication and thermal management of 2D heterostructures (see Figure 4.4). This coefficient is difficult to measure and most studies rely on simulations. A new experimental approach has been reported, which characterizes this thermal coefficient in suspended MoS_2 using micro-Raman spectroscopy [87].
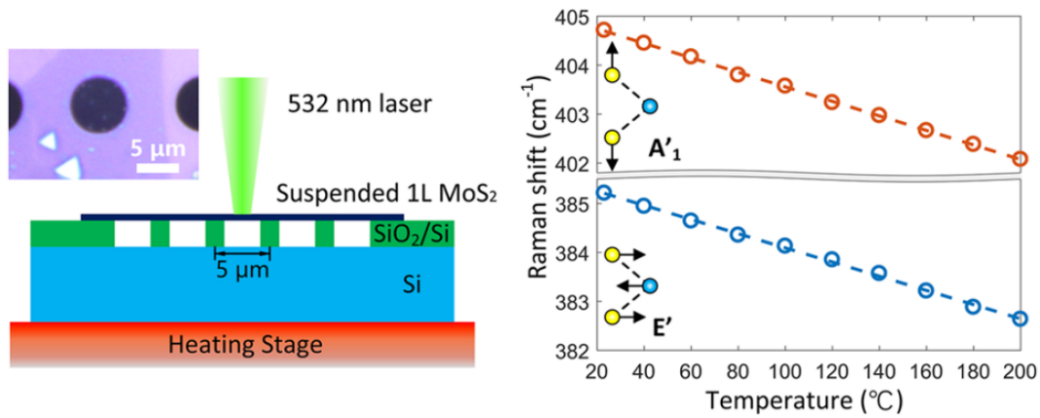
Figure 4.4: Thermal expansion coefficient of monolayer MoS_2. (a) Diagram of suspended monolayer MoS_2 over 3 μm long trenches patterned in SiO_2. Inset: Optical image of suspended device. (b) Temperature dependence of the Raman peak shift (y-axis). Inset: (top) A'$_1$ Raman mode and (bottom) E' mode. Figure reproduced from [87]

In conclusion, we presented a 2D heterostructure transfer assembly method based on a nitrocellulose micro-stamp which is able to stamp 2DMs (SLG, BLG, FLG, hBN, MoS2) in any-stacking order and incorporate suspended 2DMs. It was shown to dry pick-up 2DMs directly from SiO_2 substrates, and transfer them with micron precision alignment. The full procedure takes under 60 minutes and has a success rate around 95%. It can be used to transfer suspended ultra-thin materials such as monolayer and bilayer graphene over areas up to 10 μm^2 and height as low as 550 nm without requiring a critical point drying process. No visible Raman disorder, macroscopic tear or significant bubbles are seen in the transferred crystals. We demonstrate the assembly of planar heterostructure optical cavities able to broadly tune the Raman scattering by a factor of up to 19, and underlying light absorption by a similar amount, in both supported and suspended BLG. Our fabrication method fills a major gap in previous transfer method by enabling the flexible transfer of suspended 2DMS (any 2DMs, stacking-order, substrate) all the way down to the ultra-thin 2DM limit (SLG, BLG). We foresee that this fabrication route can create 2D heterostructures suited for exploring the interplays of nanoscale mechanics, optics, and electronics, for instance in twisted bilayer graphene [17].

Appendix

Link to Stamping Transfer Movie 1

```
https://drive.google.com/file/d/1fxRgk1a6Nn12cdaN7jFEiIlFFgCM4m9p/
view?usp=sharing
```

Contrast

In order to locate graphene on a SiO_2 substrate by an optical microscope, the thickness of SiO_2 is carefully chosen to increase the contrast between them. This thickness is in the same order of magnitude as the wavelength of the incident light, therefore, interference effects must be accounted for. We use a model based on Fresnel's equations to determine the exact thickness of SiO_2 to be used to maximize this contrast.

$$C = \frac{I(n_{\text{air}}) - I(n_{\text{Gr}})}{I(n_{\text{air}})} \tag{4.1}$$

Where, $I(n_{\text{air}})$ is the intensity of reflected light in the absence of graphene and $I(n_{\text{Gr}})$ is the intensity of reflected light in the presence of graphene [60].

We can see in figure 2.8a the optical images of graphene on SiO_2 of different thickness and with different wavelengths. Under white light is clear that a thickness of about 300 nm is ideal to be used. In part b we see a color plot of the contrast as a function of wavelength and thickness. Our wafers are made of 500 μm of Si and 310 nm of SiO_2 and have a photolithography patterned grid for easier location of candidate crystals to be stamped.
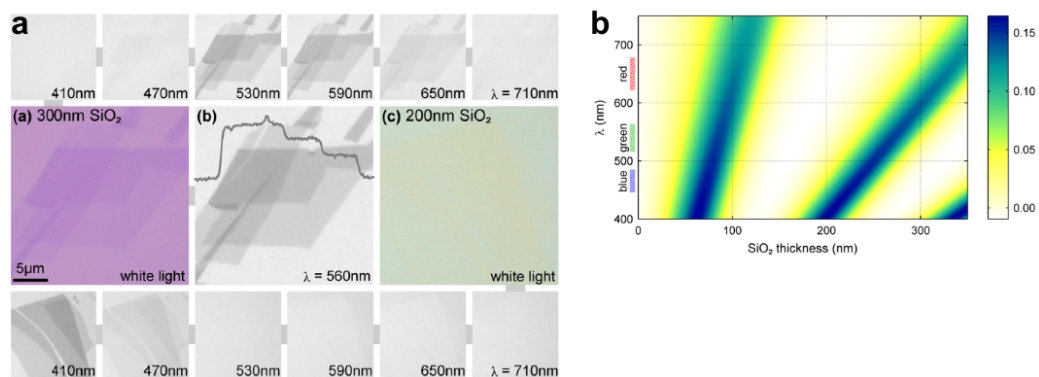
Figure 4.5: Graphene contrast with background. (a) Graphene crystal on 300 nm SiO2 imaged with white light, SLG is clearly visible (a). (b) Same crystal under green light and the trace shows step-like changes in the contrast for 1, 2, and 3 layers. (c) Another graphene sample on 200 nm SiO2 under white light, where even three layers are indiscernible. Top and bottom panels show the same flakes as in (a) and (c), respectively, but illuminated through various narrow bandpass filters with a bandwidth of 10 nm. The flakes were chosen to contain areas of different thickness so that one can see changes in graphene's visibility with increasing numbers of layers. This proves that the contrast can also be used as a quantitative tool for defining the number of graphene layers on a given substrate. Figure reproduced from [60].

hBN Crystal Characterization
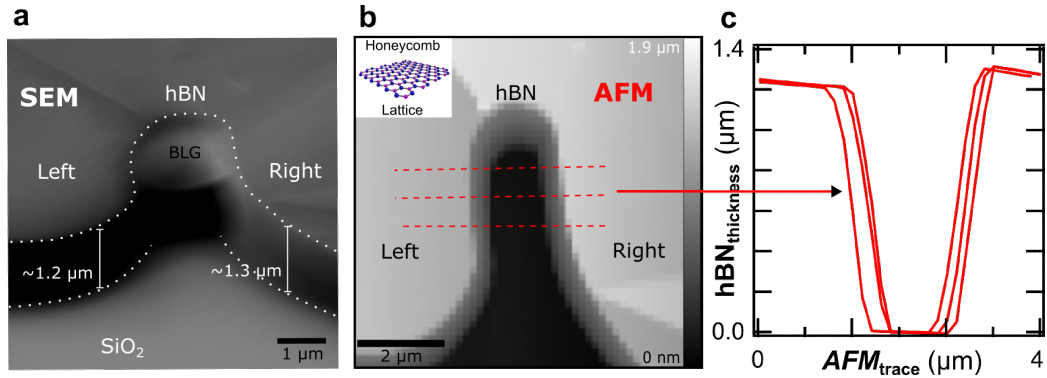
Figure 4.6: Complete characterization of hBN trench that works as new substrate. (a) Titled SEM image (60 degrees) with approximated thickness measurement (white solid lines), dotted white lines as a guide to the eye. (b) AFM scan image with line traces (red dotted lines) over the cavity region to measure its thickness. (c) Plot of hBN thickness as a function of AFM trace position for all traces in (b).

AFM measurement of the hBN-spacer thickness are performed at the region where the BLG crystals are located to minimized uncertainty (figure 3.15). Device A1 has a hBN-spacer thickness of 370 nm, A2 of 385 nm, A3 of 435 nm and A4 of 445nm nm. The error bar on these hBN-spacer thickness is about $\pm$ 10 nm, which correspond to 2.7%, 2.6%, 2.3% and 2.2% respectively.
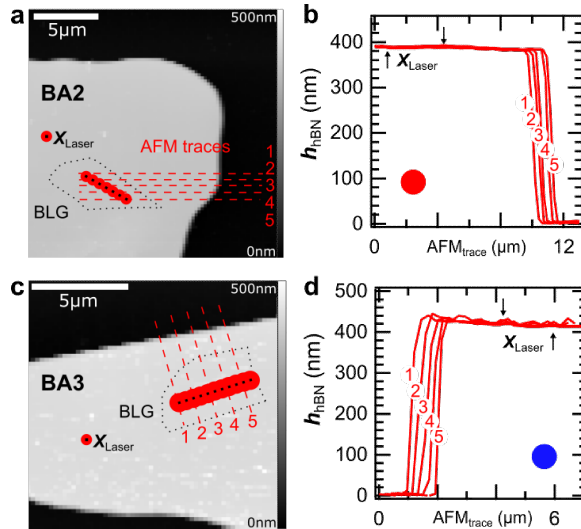
Figure 4.7: AFM measurement of hBN thickness in devices A2-3

Derivation of Fresnel's equations

Fresnel's equations (or Fresnel's coefficients) describe the reflection and transmission of electromagnetic radiation when incident on an interface between different optical media. They are derived from the boundary conditions of the electric and magnetic fields [69]:

$$\vec{E}_{1\parallel} = \vec{E}_{2\parallel} \tag{4.2}$$

$$\varepsilon_1 \vec{E}_{1\perp} = \varepsilon_2 \vec{E}_{2\perp} \tag{4.3}$$

$$\frac{\vec{B}_{1\parallel}}{\mu_1} = \frac{\vec{B}_{2\parallel}}{\mu_2} \tag{4.4}$$

$$\vec{B}_{1\perp} = \vec{B}_{2\perp} \tag{4.5}$$

$$\vec{E} = E_0 cos(kx - \omega t + \phi) \tag{4.6}$$

$$B_0 = \frac{E_0}{\upsilon} \tag{4.7}$$

The polarization of an electromagnetic wave refers to the direction of the E-field. For p-polarized light, the E-field is parallel to the plane of incidence while for s-polarized, it is perpendicular to the plane of incidence. From the boundary conditions, we have

$$E_{0i}cos(\theta_i) - E_{0r}cos(\theta_r) = E_{0t}cos(\theta_t) \tag{4.8}$$

$$\frac{1}{\mu_i v_i} E_{0i} + \frac{1}{\mu_r v_r} E_{0r} = \frac{1}{\mu_t v_t} E_{0t} \tag{4.9}$$

and

$$\mu_i = \mu_r \approx \mu_t \approx \mu_0, \theta_i = \theta_r, \frac{1}{\mu v} = \frac{n}{\mu c} \tag{4.10}$$

We then define the amplitude reflection coefficient for p and s-polarized light (i, r, t subscripts mean incident, reflected and transmitted):

$$r_p \equiv \left(\frac{E_{0r}}{E_{0i}}\right)_\| = \frac{n_i cos(\theta_t) - n_t cos(\theta_i)}{n_i cos(\theta_t) + n_t cos(\theta_i)} \tag{4.11}$$

$$r_s \equiv \left(\frac{E_{0r}}{E_{0i}}\right)_\perp = \frac{n_i cos(\theta_i) - n_t cos(\theta_t)}{n_i cos(\theta_i) + n_t cos(\theta_t)} \tag{4.12}$$

and for the amplitude transmission coefficient:

$$t_p \equiv \left(\frac{E_{0t}}{E_{0i}}\right)_\| = \frac{2 n_i cos(\theta_i)}{n_i cos(\theta_t) + n_t cos(\theta_i)} \tag{4.13}$$

$$t_s \equiv \left(\frac{E_{0t}}{E_{0i}}\right)_\perp = \frac{2 n_i cos(\theta_t)}{n_i cos(\theta_i) + n_t cos(\theta_t)} \tag{4.14}$$

Derivation of recursive method

We can get the reflection coefficient by summing up all contributions (see figure 4.8),

$$r_{3media} = r_{01} + t_{10} r_{12} t_{01} e^{i2\beta_1} + t_{10} r_{12} r_{10} r_{12} t_{01} e^{2(2i\beta_1)} + t_{10} (r_{12} r_{10})^2 r_{12} t_{01} e^{4(2i\beta_1)} \tag{4.15}$$
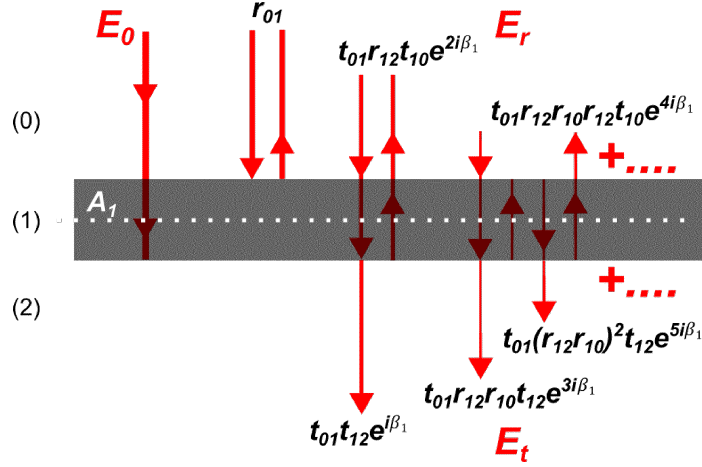
Figure 4.8: Contributing terms

$$r_{3\text{media}} = r_{01} + t_{10}r_{12}t_{01}e^{2i\beta_1}\left(1 + r_{10}r_{12}e^{2i\beta_1} + (r_{10}r_{12})^2 e^{2(2i\beta_1)}\right)$$

Let $a = t_{10}r_{12}t_{01}e^{2i\beta_1}$ and $z = r_{10}r_{12}e^{2i\beta_1}$, this way we can represent this as an infinite complex geometric series,

$$r_{3\text{media}} = r_{01} + (a + az + az^2 + ...) = r_{01} + \left(\frac{a}{a-z}\right)$$

Replacing back a and z, and using Stokes relationships $r_{i,j} = -r_{i,j}$ and $r_{i,j}r_{j,i} - t_{i,j}t_{j,i} = -1$, we get equation 4.18,

$$r_{3\text{media}} = \frac{r_{01} + r_{12}e^{2i\beta_1}}{1 + r_{12}r_{01}e^{2i\beta_1}}$$

In the same way we can sum up the transmission coefficient contributions to get equation 4.19.

We can think of r_{12} as an effective reflection coefficient in equation 4.18, therefore we can the reflection coefficient for 4 media.

$$r_{4\text{media}} = \frac{r_{01} + r_{3\text{media}}e^{2i\beta_1}}{1 + r_{01}r_{3\text{media}}e^{2i\beta_1}}$$

$$r_{4\text{media}} = \frac{r_{01} + r_{12}e^{2i\beta_1} + [r_{12} + r_{12}e^{2i\beta_1}]r_{23}e^{2i\beta_2}}{1 + r_{01}r_{01}e^{2i\beta_1} + [r_{12} + r_{12}e^{2i\beta_1}]r_{23}e^{2i\beta_2}}$$

We can think of t_{12} as an effective transmission coefficient in equation 4.19, therefore we can the transmission coefficient for 4 media.

$$t_{4\text{media}} = \frac{t_{01}t_{3\text{media}}e^{i\beta_1}}{1 + r_{01}r_{3\text{media}}e^{2i\beta_1}}$$

$$t_{4\text{media}} = \frac{t_{01}t_{12}t_{23}e^{i(\beta_1+\beta_2)}}{1 + r_{01}r_{12}e^{2i\beta_1} + [r_{12} + r_{12}e^{2i\beta_1}]r_{23}e^{2i\beta_2}}$$

Derivation of transfer matrix method

A transfer matrix method is used to compute the electric fields at different depths in multilayer systems. We assume a partial wave propagating as a harmonic plane wave of the form,

$$E(\vec{r}, t) = E_0 exp\left(i[\vec{k} \cdot \vec{r} - \omega t]\right) \tag{4.16}$$

Within a medium the x, y and time dependence is the same, therefore, we only track the z-component. The electric field in each medium is composed of forward (+) and backward (-) propagating waves,

$$E = E^{(+)} + E^{(-)} \tag{4.17}$$

This can also be defined as a 2x1 column matrix,

$$E(z) = \begin{bmatrix} E^{(+)}(z) \\ E^{(-)}(z) \end{bmatrix} \tag{4.18}$$

The total matrix S connects the electric field amplitudes above the first interface and below the last interface,
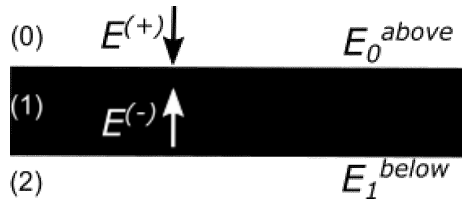
Figure 4.9: Electric fields

$$S \cdot E_{\text{n}}^{\text{below}} = E_0^{\text{above}} \tag{4.19}$$

Given that the incident light comes from above,

$$\begin{bmatrix} S_{11} & S_{12} \\ S_{21} & S_{22} \end{bmatrix} \cdot \begin{bmatrix} E_{\text{t}}^{\text{n}} \\ 0 \end{bmatrix} = \begin{bmatrix} E_{\text{i}}^0 \\ E_{\text{r}}^0 \end{bmatrix} \tag{4.20}$$

The total transfer matrix is composed of two individual matrices, interface and propagation.

$$S = I_{01} \cdot L_1 \cdot I_{12} \cdot L_2 \cdot .... \cdot I_{\text{n-1,n}} \cdot L_{\text{n}} \cdot I_{\text{n,n+1}} \tag{4.21}$$

The interface matrix connects the electric fields above and below an interface and is defined as,

Put transfer matrix fig

$$I_{\text{n,n+1}} \cdot E_{\text{n}}^{\text{below}} = E_{\text{n}}^{\text{above}} \tag{4.22}$$

$$\begin{bmatrix} I_{11} & I_{12} \\ I_{21} & I_{22} \end{bmatrix} \cdot \begin{bmatrix} E_{\text{below}}^{(+)} \\ E_{\text{below}}^{(-)} \end{bmatrix} = \begin{bmatrix} E_{\text{above}}^{(+)} \\ E_{\text{above}}^{(-)} \end{bmatrix}$$

Figure 4.10: Interface and propagation matrices

The forward propagating wave (transmitted) below the interface is given by,

$$E_{\text{below}}^{(+)} = t_{01} E_{\text{above}}^{(+)} + r_{10} E_{\text{below}}^{(-)}$$

The backward propagating wave (reflected) above the interface is,

$$E_{\text{above}}^{(-)} = r_{01} E_{\text{above}}^{(+)} + t_{10} E_{\text{below}}^{(-)}$$
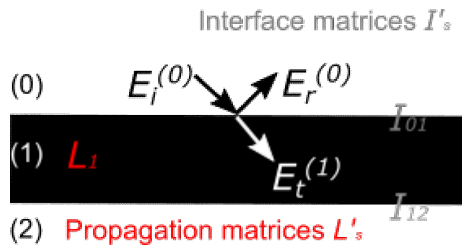
After some algebra we have,

$$E_{\text{above}}^{(+)} = \frac{E_{\text{below}}^{(+)} + r_{10} E_{\text{below}}^{(-)}}{t_{01}}$$

$$E_{\text{above}}^{(-)} = \frac{r_{01}}{t_{01}} E_{\text{below}}^{(+)} + \left(\frac{r_{01}^2}{t_{01}} + t_{01} \right) E_{\text{below}}^{(-)} = \frac{1}{t_{01}} \left(r_{01} E_{\text{below}}^{(+)} + E_{\text{below}}^{(-)} \right)$$

Therefore, the interface matrix is,

Put interface matrix fig

$$I_{\text{n,n+1}} = \frac{1}{t_{\text{n,n+1}}} \begin{bmatrix} 1 & r_{\text{n,n+1}} \\ r_{\text{n,n+1}} & 1 \end{bmatrix} \tag{4.23}$$

The propagation matrix is,

$$L_{\text{n}} \cdot E_{\text{n}}^{\text{above}} = E_{\text{n-1}}^{\text{below}} \tag{4.24}$$

$$\begin{bmatrix} L_{11} & L_{12} \\ L_{21} & L_{22} \end{bmatrix} \cdot \begin{bmatrix} E_{\text{above (n)}}^{(+)} \\ E_{\text{above(n)}}^{(-)} \end{bmatrix} = \begin{bmatrix} E_{\text{below(n-1)}}^{(+)} \\ E_{\text{below(n-1)}}^{(-)} \end{bmatrix}$$
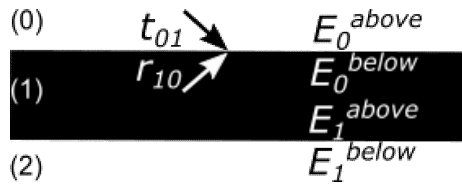

Figure 4.11: Interface matrix

The forward and backward propagating waves are,

$$E_{\text{above(n)}}^{(+)} = E_{\text{below(n-1)}}^{(+)} \cdot e^{-i\beta}$$

$$E_{\text{below(n-1)}}^{(-)} = E_{\text{above(n)}}^{(-)} \cdot e^{i\beta}$$

Therefore, the propagation matrix is,

$$L_{\text{n}} = \begin{bmatrix} e^{-i\beta_{\text{n}}} & 0 \\ 0 & e^{i\beta_{\text{n}}} \end{bmatrix} \tag{4.25}$$
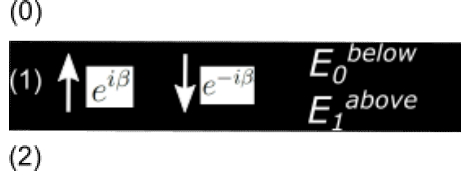
Figure 4.12: Propagation matrix

For the case of tree media we have a total matrix S,

$$S = I_{01} \cdot L_1 \cdot I_{12} \tag{4.26}$$

$$= \frac{1}{t_{01}t_{12}} \begin{bmatrix} 1 & r_{01} \\ r_{01} & 1 \end{bmatrix} \cdot \begin{bmatrix} e^{-i\beta_1} & 0 \\ 0 & e^{i\beta_1} \end{bmatrix} \cdot \begin{bmatrix} 1 & r_{12} \\ r_{12} & 1 \end{bmatrix}$$

$$= \frac{1}{t_{01}t_{12}} \begin{bmatrix} r_{01}r_{12}e^{i\beta_1} + e^{-i\beta_1} & r_{01}e^{i\beta_1} + r_{12}e^{-i\beta_1} \\ r_{01}e^{-i\beta_1} + r_{12}e^{i\beta_1} & r_{01}r_{12}e^{-i\beta_1} + e^{i\beta_1} \end{bmatrix}$$

The reflection and transmission coefficients can be found using,

$$r_{\text{3media}} = \frac{E_r}{E_i} = \frac{S_{21}}{S_{11}}$$

$$= \frac{r_{01} + r_{12}e^{2i\beta_1}}{1 + r_{01}r_{12}e^{2i\beta_1}} \tag{4.27}$$

$$t_{\text{3media}} = \frac{E_t}{E_i} = \frac{1}{S_{11}}$$

$$= \frac{t_{01}t_{12}e^{i\beta_1}}{1 + r_{01}r_{12}e^{2i\beta_1}} \tag{4.28}$$

76

For 4 media we get the coefficients to be,
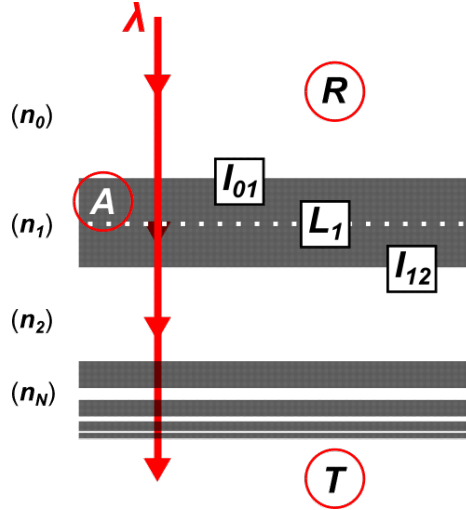
Figure 4.13: All matrices

$$r_{4\text{media}} = \frac{r_{01} + r_{12}e^{2i\beta_1} + [r_{12} + r_{12}e^{2i\beta_1}]r_{23}e^{2i\beta_2}}{1 + r_{01}r_{01}e^{2i\beta_1} + [r_{12} + r_{12}e^{2i\beta_1}]r_{23}e^{2i\beta_2}} \qquad (4.29)$$

$$t_{4\text{media}} = \frac{t_{01}t_{12}t_{23}e^{i(\beta_1+\beta_2)}}{1 + r_{01}r_{12}e^{2i\beta_1} + [r_{12} + r_{12}e^{2i\beta_1}]r_{23}e^{2i\beta_2}} \qquad (4.30)$$

Derivation of Raman factor

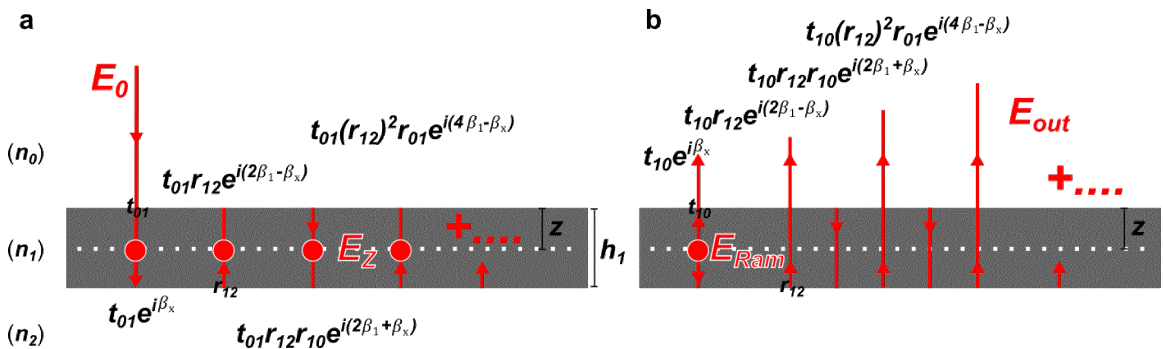Figure 4.14: Contributing terms

The Raman interaction happens in the graphene layer. The ratio of the incoming electric field at the position z and the incoming one can be expressed as,

$$\frac{E_z}{E_0} = t_{01}(e^{-i\beta_z} + r_{12}e^{-i(2\beta_1-\beta_z)} + r_{12}r_{10}e^{-i(2\beta_1+\beta_z)} + r_{12}^2 r_{10}e^{-i(4\beta_1-\beta_z)} + r_{12}^2 r_{10}^2 e^{-i(4\beta_1+\beta_z)} + ...)$$

Set $c = r_{12}r_{10}e^{-i2\beta_1}$ and factor it out. By grouping the even and odd terms and using the relationship $1 + c + c^2 + c^3 + ... + c^n = (1 - c^{n+1}/1 - c)$ that is valid for complex number c. We can simplify,

$$\frac{E_z}{E_0} = t_{01}(e^{-i\beta_z}[\frac{1-(r_{12}r_{10}e^{-2i\beta_1})^{n+1}}{1-r_{12}r_{10}e^{-2i\beta_1}}] + r_{12}e^{-i(2\beta_1-\beta_z)}[\frac{1-(r_{12}r_{10}e^{-2i\beta_1})^{n+1}}{1-r_{12}r_{10}e^{-2i\beta_1}}])$$

As $n \to \infty$, we get,

$$(r_{12}r_{10}e^{-2i\beta_1})^{n+1} \to 0$$

Caring the multiplication,

$$F_{ab,3media} = \frac{E_z}{E_0} = t_{01}\frac{e^{-i\beta_z} + r_{12}e^{-i(2\beta_1-\beta_z)}}{1 + r_{12}r_{10}e^{-2i\beta_1}} \tag{4.31}$$

The same happens to be true when summing up all components to get the electric field outside, in other words, the Raman signal detected by the spectrometer

$$F_{sc,3media} = \frac{E_{out}}{E_{Ram}} = t_{10}\frac{e^{-i\beta_z} + r_{12}e^{-i(2\beta_1-\beta_z)}}{1 + r_{12}r_{10}e^{-2i\beta_1}} \tag{4.32}$$

The ratios E_z/E_0 and E_R/E_{out} are the net absorption and Raman scattering terms. The total enhancement factor of the measured Raman signal is calculated by integrating the ratios product over the graphene thickness h_l,

$$F_{Gr} = N \int_0^{h_l} \left| \frac{E_z}{E_0} \cdot \frac{E_{out}}{E_{Ram}} \right|^2 dz \tag{4.33}$$

Where N is the normalization constant. This constant is found for the case where

a monolayer graphene is surrounded by vacuum, this is the intrinsic Raman intensity when no interference effects are present.

For the case with 4 media, the equations are,

$$F_{\text{ab,4media}} = t_{01} \frac{[1 + r_{12}r_{23}e^{-2i\beta_2}]e^{-i\beta_z} + [r_{12} + r_{23}e^{-2i\beta_2}]e^{-i(2\beta_1 - \beta_z)}}{1 + r_{12}r_{23}e^{-2i\beta_2} + [r_{12} + r_{23}e^{-2i\beta_2}]r_{01}e^{-2i\beta_1}} \tag{4.34}$$

$$F_{\text{sc,4media}} = t_{10} \frac{[1 + r_{12}r_{23}e^{-2i\beta_2}]e^{-i\beta_z} + [r_{12} + r_{23}e^{-2i\beta_2}]e^{-i(2\beta_1 - \beta_z)}}{1 + r_{12}r_{23}e^{-2i\beta_2} + [r_{12} + r_{23}e^{-2i\beta_2}]r_{01}e^{-2i\beta_1}} \tag{4.35}$$

Bibliography

[1] R. Frisenda, E. Navarro-Moratalla, P. Gant, D.P. De Lara, P. Jarillo-Herrero, R.V. Gorbachev, and A. Castellanos-Gomez. Recent Progress in the Assambly of Nanodevices and van der Waals Heterostructure by Deterministic Placement of 2D Materials. *Chemical Society Reviews*, 47:53–68, 2018.

[2] S. Fan, Q.A. Vu, M.D. Tran, S. Adhikari, and Y.H Lee. Transfer Assembly for Two-Dimensional van der Waals Heterostructures. *2D Materials*, 7(022005), 2016.

[3] K.S. Novoselov, A. Mishchenko, A. Carvalho and A.H. Castro Neto. 2D Materials and van der Waals Heterostructures. *Science*, 353(6298), 2016.

[4] Y. Liu, Y. Huang, and X. Duan. Van der Waals Integration Before and Beyond Two-Dimensional Materials. *Nature*, 567:323-333, 2019.

[5] B. Li, J. Yin, X. Liu, H. Wu, J. Li, X. Li, and W. Guo. Probing van der Waals Interactions at Two-Dimensional Heterointerfaces. *Nature Nanotechnology*, 14:567–572, 2019.

[6] M. Yankowitz, Q. Ma, P. Jarillo-Herrero, and B. J. LeRoy. Van der Waals Heterostructures Combining Graphen and Hexagonal Boron Nitride. *Nature Reviews Physics*, 1, 112-125, 2019.

[7] J.C.W. Song, and N.M. Gabor. Electron Quantum Metamaterials in Van der Waals Heterostructures. *Nature Nanotechnology*, 13:986–993, 2018.

[8] P. Rivera, H. Yu, K.L. Seyler, N.P. Wilson, W. Yao, and X. Xu. Interlayer Valley Excitons in Heterobilayers of Transition Metal Dichalcogenides. *Nature Nanotechnology*, 13:1004–1015, 2018.

[9] T. Deilmann, M. Rohlfing, and U. Wurstbauer.Light–Matter Interaction in van der Waals Hetero-Structures. *Journal of Physics: Condensed Matter*, 32(333002), 2020.

[10] A. Castellanos-Gomez, M. Buscema, R. Molenaar, V. Singh, L. Janssen, H.S.J. van der Zant, and G.A. Steele. Deterministic Transfer of Two-Dimensional Materials by All-Dry Viscoelastic Stamping. *IOPS 2D Materials*, 1(1), 2014.

[11] V. Singh, S. J. Bosman, B. H. Schneider, Y. M. Blanter, A. Castellanos-Gomez, and G. A. Steele. Optomechanical Coupling Between a Multilayer Graphene Mechanical Resonator and a Superconducting Microwave Cavity. *Nature Nanotechnology*, 9:820–824, 2014.

[12] L. Midolo, A. Schliesser, and A. Fiore. Nano-Opto-Electro-Mechanical Systems. *Nature Nanotechnology*, 13:11–18, 2018.

[13] M. Florian, M. Hartmann, A. Steinhoff, J. Klein, A. W. Holleitner, J. J. Finley, T. O. Wehling, M. Kaniber, and C. Gies. The Dielectric Impact of Layer Distances on Exciton and Trion Binding Energies in van der Waals Heterostructures. *Nano Lettres*, 18:2725–2732, 2018.

[14] K. Kim, M. Yankowitz, B. Fallahazad, S. Kang, H.C.P. Movva, S. Huang, S. Larentis, C.M. Corbet, T. Taniguchi, K. Watanabe, S.K. Banerjee, and B.J. LeRoy. van der Waals Heterostructures with High Accuracy Rotational Alignment. *Nano Lett.*, 3:1989–1995, 2016.

[15] A. C. McRae, G. Wei, and A. R. Champagne. Graphene Quantum Strain Transistors *Physical Review Applied*, 11, 2019.

[16] X. Zhang, K. Markles, L. Colombier, D. Metten, H. Majjad, P. Verlot, and S. Berciaud. Dinamically-Enhanced Strain in Atomically-Thin Resonators. *arXiv*, preprint arXiv:2003.11167, 2020.

[17] Y. Cao, V. Fatemi, S. Fang, K. Watanabe, T. Taniguchi, E. Kaxiras, and P. Jarillo-Herrero. Unconventional Superconductivity in Magic-Angle Graphene Superlattices *Nature* 556:43–50, 2018.

[18] L. Xian, D.M. Kennes, N. Tancogne-Dejean, M. Altarelli, and A. Rubio. Multiflat Bands and Strong Correlations in Twisted Bilayer Boron Nitride: Doping-Induced Correlated Insulator and Superconductor. *Nano Letters*, 8:4934–4940, 2019.

[19] H. Song, S. Jiang, D. Ji, X. Zeng, N. Zhang, K. Liu, C. Wang, Y. Xu, and Q. Gan. Nanocavity Absorption Enhancement for Two-Dimensional Material Monolayer Systems. *Optics Express*, 23(6):7120–7130, 2015.

[20] I. Epstein, B. Terrs, A. J. Chaves, V. V. Pusapati, D. A. Rhodes, B. Frank, V. Zimmermann, Y. Qin, K. Watanabe, T. Taniguchi, H. Giessen, S. Tongay, J. C. Hone, N. M. R. Peres, and F. H. L. Koppens. Near-Unity Light Absorption in a Monolayer WS2 Van der Waals Heterostructure Cavity. *Nano Letters*, 20:3545–3552, 2020.

[21] M. Casalino, U. Sassi, I. Goykhman, A. Eiden, E. Lidorikis, S. Milana, D. De Fazio, F. Tomarchio, M. Iodice, G. Coppola, and A. C. Ferrari. Vertically Illuminated, Resonant Cavity Enhanced, Graphene-Silicon Schottky Photodetectors. *ACS Nano*, 11:10955–10963, 2017.

[22] B. J. Eggleton, C. G. Poulton, P. T. Rakich, M. J. Steel, and G. Bahl. Brillouin Integrated Photonics. *Nature Photonics*, 13:664–677, 2019.

[23] C. Haffner, A. Joerg, M. Doderer, F. Mayor, D. Chelladurai, Y. Fedoryshyn, C. I. Roman, M. Mazur, M. Burla, H.J. Lezec, V. A. Aksyuk, and J. Leuthold. Nano–Opto-Electro-Mechanical Switches Operatedat CMOS-Level Voltages. *Science*, 366:860–864, 2019.

[24] X. Zhang, C. De-Eknamkul, J. Gu, A.L. Boehmke, V.M. Menon, J. Khurgin, and E. Cubukcu. Guiding of Visible Photons at the Angstrom Thickness Limit. *Nature Nanotechnology*, 14:844–850, 2019.

[25] D. Jariwala, T.J. Marks, and M.C. Hersam. Mix-Dimensional van der Waals Heterostructures. *Nature Materials*, 16:170–181, 2017.

[26] A.K. Geim, and I.V. Grigorieva. Van der Waals Heterostructures. *Nature*, 499:419-425, 2013.

[27] F. Pizzocchero, L. Gammelgaard, B.S. Jessen, J.M. Caridad, L. Wang, J. Hone, P. Boggid, and T.J. Booth. The Hot Pick-Up Technique for Batch Assembly of van der Waals Heterostructures. *Nature Comm.*, 7(1):11894, 2016.

[28] R. Xiang, T. Inoue, Y. Zheng, A. Kumamoto, Y. Qian, Y. Sato, M. Liu, D. Tang, D. Gokhale, J. Guo, K. Hisama, S. Yotsumoto, T. Ogamoto, H. Arai, Y. Kobayashi, H. Zhang, B. Hou, A. Anisimov, M. Maruyama, Y. Miyata, S. Okada, S. Chiashi, Y. Li, J. Kong, E.I. Kauppinen, Y. Ikuhara, K. Suenaga, and S. Maruyama. One Dimensional van der Waals Heterostructures. *Science*, 367(6477), 2020.

[29] S.J. Yang, S. Choi, F.O.O. Ngome, K.J. Kim, S.Y. Choi, and C.J. Kim. All-Dry Transfer of Graphene Film by van der Waals Interactions. *Nano Letters*, 6:3590–3596, 2019.

[30] K. Kinoshita, R. Moriya, M. Onodera, Y. Wakafuji, S. Masubuchi, K. Watanabe, T. Taniguchi, and T. Machida. The Hot Pick-Up Technique for Batch Assembly of van der Waals Heterostructures. *Nature 2D Materials*, 3(22), 2019.

[31] L. Tao, H. Li, Y. Gao, Z. Chen, L. Wang, Y. Deng, J. Zhang and J.B. Xu. Deterministic and Etching-Free Transfer of Large-Scale 2D Layered Materials for Constructing Interlayer Coupled van der Waals Heterostructures. *Adv. Mater. Techol.*, 3(1700282), 2018.

[32] T. Uwanno, Y. Hattori, T. Taniguchi, K. Watanabe, and K. Nagashio. Fully Dry PMMA Transfer of Graphene on h-BN Using a Heating/Cooling System. *2D Materials*, 2(4), 2015.

[33] T. Volkl, T. Rockinger, M. Drienovsky, K. Watanabe, T. Taniguchi, D. Weiss, and J. Eroms. Magnetotransport in Heterostructures of Transition Metal Dichalcogenides and Graphene. *Physical Review B*, 96(125405), 2017.

[34] X. Ma, Q. Liu, D. Xu, Y. Zhu, S. Kim, Y. Cui, L. Zhong, and M. Liu. Capillary-Force-Assisted Clean-Stamp Transfer of Two-Dimensional Materials. *Nano Letters*, 11:6961–6967, 2017.

[35] S.K. Roy, V.T.K. Sauer, J.N. Westwood-Bachman, A. Venkatasubramanian, and W.K. Hiebert. Improving Mechanical Sensor Performance Through Larger Damping. *Science*, 360(6394), 2018.

[36] S.J. Kim, T. Choi, B. Lee, S. Lee, K. Choi, J.B. Park, J.M. Yoo, Y.S. Choi, J. Ryu, P. Kim, J. Hone and B.H. Hong. Ultraclean Patterned Transfer of Single-Layer Graphene by Recyclable Pressure Sensitive Adhesive Films. *Nano Lett.*, 5:3236–3240, 2015.

[37] Y. Liu, T.S. Abhilash, A. Laitinen, Z. Tan, G.J. Liu, and P. Hakonen. Dry Transfer Method for Suspended Graphene on Lift-off-Resist: Simple Ballistic Devices with Fabry-Perot Interference. *IOPS 2D Materials*, 30(25), 2019.

[38] O. Zheliuk, J.M. Lu, Q.H. Chen, A.A. El Yumin, S. Golightly, and J.T. Ye. Josephson Coupled Ising Pairing Induced in Suspended MoS_2 Bilayers by Double-Side Ionic Gating. *Nature Nanotechnology*, 14:1123–1128, 2019.

[39] S. Yigen. Electronic Thermal Conductivity Measurements in Graphene. *M.Sc. Thesis*, 33–36, 2015.

[40] D. Ji, S. Cai, T.R. Paudel, H. Sun, C. Zhang, L. Han, Y. Wei, Y. Zang, W. Gao, H. Huyan, W. Guo, D. Wu, Z. Gu, E.Y. Tsymbal, P. Wang, Y. Nie, and X. Pan. Freestanding Crystalline Oxide Perovskites Down to the Monolayer Limit. *Nature*, 570:87–90, 2019.

[41] A. H. Castro Neto. The Electronic Properties of Graphene. *Review of Modern Physics*, 81(109), 2009.

[42] J. Nilsson, A. H. Castro Neto, F. Guinea, and N. M. R. Peres. The Electronic Properties of Graphene Multilayers. *Physical Review Letters*, 97(266801), 2006.

[43] I. Al-Naib, J. E. Sipe, and M. M. Dignam. High Harmonic Generation in Undoped Graphene: Interplay of Inter- and Intraband Dynamics. *Physical Review B*, 90(245423), 2014.

[44] F. Bonaccorso, Z. Sun, T. Hasan, and A.C. Ferrari Graphene Photonics and Optoelectronics. *Nature Photonics*, 4:611–622, 2010.

[45] R.R. Nair, P. Blake, A.N. Grigorenko, K.S. Novoselov, T.J. Booth, T. Stauber, N.M.R. Peres, and A.K. Geim. Universal Dynamic Conductivity and Quantized Visible Opacity of Suspended Graphene. *Science*, 320(1308), 2008.

[46] M.S. Dresselhaus Solid State Physics II, Optical Properties of Solids. *MIT Lectures*, 2–17, 2010.

[47] A.C. Ferrari, J.C. Meyer, V. Scardaci, C. Casiraghi, M. Lazzeri, F. Mauri, S. Piscanec, D. Jiang, K.S. Novoselov, S. Roth, and A.K. Geim. Raman Spectrum of Graphene and Graphene Layers. *Physical Review Letters*, 97(187401), 2006.

[48] A.C. Ferrari, and D.M. Basko. Raman Spectroscopy as a Versatile Toll for Studing the Properties of Graphene. *Nature Nanotechnology*, 8:235–246, 2013.

[49] M.S. Dresselhaus, A. Jorio, and R. Saito Characterizing Graphene, Graphite and Carbon Nanotubes by Raman Spectrocopy. *Annual Review of Condensed Matter Physics*, 1(1):89–108, 2010.

[50] R.J. Shiue, Y. Gao, C. Tan, C. Peng, J. Zheng, D.K. Efetov, Y.D. Kim, J. Hone, and D. Englund. Thermal Radiation Control from Hot Graphene Electrons Coupled to a Photonic Crystal Nanocavity. *Nature Communications*, 10(109), 2019.

[51] S. Maiti, and D.L. Maslov. Raman Scattering in a Two-Dimensional Fermi Liquid with Spin-Orbit Coupling. *Physical Review B*, 95(134425), 2017.

[52] M.S. Dresselhaus, and G. Dresselhaus Intercalation Compounds of Graphite . *Advances in Physics*, 30:139–326, 1980.

[53] L.M. Malard, M.A. Pimenta, G. Dresselhaus, and M.S. Dresselhaus. Raman Spectroscopy in Graphene. *Elsevier Physics Reports*, 473(5-6):51-87, 2009.

[54] B. Li, Y. He, S. Lei, S. Najmaei, Y. Gong, X. Wang, J. Zhang, L. Ma, Y. Yang, S. Hong, J. Hao, G. Shi, A. George, K. Keyshar, X. Zhang, P. Dong, P. Dong, L. Ge, R. Vajtai, J. Lou, Y.J. Jung, and P.M. Ajayan. Scalable Transfer of Suspended Two-Dimensional Single Crystals. *Nano Lett.*, 8:5089–5097, 2015.

[55] G. Froehlicher, and S. Berciaud. Raman Spectroscopy of Electrochemically-Gated Graphene Transistors: Geometrical Capacitance, Electron-Phonon,

Electron-Electron, and Electron-Defect Scattering. *Physical Review B*, 91(205413), 2015.

[56] J. B. Wu, M. L. Lin, X. Cong, H. N. Liua, and P. H. Tan. Raman Spectroscopy of Graphene-based Materials and its Applications in Related Devices. *Chemical Society Review*, 47(1822), 2018.

[57] D. Graf, F. Molitor, K. Ensslin, C. Stampfer, A. Jungen, C. Hierold, and L. Wirtz. Spacially Resolved Raman Spectroscopy of Single- and Few-Layer Graphene. *Nano Lett.*, 2:238–242, 2007.

[58] G. Iannaccone, F. Bonaccorso, L. Colombo, and G. Fiori. Quantum Engineering of Transistors Based on 2D Materials Heterostructures. *Nature Nanotechnology*, 13:183–191, 2018.

[59] X. Li, L. Tao, Z. Chen, H. Fang, X. Li, X. Wang, J.B. Xu and H. Zhu. Graphene and Related Two-Dimensional Materials: Structure-Property Relationships for Electronics and Optoelectronics. *Applied Physics Reviews*, 4(021306), 2017.

[60] P. Blake, E. W. Hill, A. H. Castro Neto, K. S. Novoselov, D. Jiang, R. Yang, T. J. Booth, and A. K. Geim. Making graphene visible. *Applied Physics Letters*, 91(6), 2007.

[61] Y. Wakafuji, R, Moriya, S. Masubuchi, K. Watanabe, T. Taniguchi, and T. Machida, T. 3D Manipulation of 2D Materials Using Microdome Polymer. *Nano Letters*, 20:2486–2492, 2020.

[62] R.A.Hemnani, j.p. Tischler, C. Carfano, R. Maiti, M.H. Tahersima, L. Bartels, R. Agarwal, And V.J. Sorger. 2D Material Printer: a Deterministic Cross Contamination-Free Transfer Method for Atomically Layered Materials. *IOPS 2D Materials*, 6(1), 2018.

[63] F. Bonaccorso, A. Lombardo, T. Hasan, Z. Sun, L. Colombo, and A. C. Ferrari. Production and Processing of Graphene and 2D Crystals. *Materials Today*, 15(12):564–589, 2012.

[64] Y. Jung, M.S. Choi, A. Nipane, A. Borah, B. Kim, A. Zangiabadi, T. Taniguchi, K. Watanabe, W.J. Yoo, J. Hone, and J.T. Teherani. Transferred via Contacts

as a Platform for Ideal Two-Dimensional Transistors. *Nature Electronics*, 2:187–194, 2019.

[65] S. Yigen, and A. R. Champagne. Wiedemann-Franz Relation and Thermal-Transistor Effect in Suspended Graphene. *Nano Letters*, 14:289–293, 2014.

[66] D. Yoon, H. Moon, Y. W. Son, J. S. Choi, B. H. Park, Y. H. Cha, Y. D. Kim, and H. Cheong. Interference Effect on Raman Spectrum of Graphene on SiO2/Si. *Physical Review B*, 80(125422), 2009.

[67] A. Nematpour, N. Lisi, A. Piegari, L. Lancellotti, G. Hu, and M.L. Grilli. Experimental Near Infrared Absorption enhancement of Graphene Layers in an Optical Resonant Cavity. *IOP Nanotechnology*, 30(44), 2019.

[68] Y. Guo, S. Jiang, X. Chen, M. Mattei, J. A. Dieringer, J. P. Ciraldo, and R. P. Van Duyne. Using a Fabry-Perot Cavity to Augment the Enhancement Factor for Surface-Enhanced Raman Spectroscopy and Tip-Enhanced Raman Spectroscopy. *Journal of Physical Chemistry*, 122:14865–14871, 2018.

[69] E. Hecht. Optics. *International edition, Addison-Wesley*, 3(2), 2002.

[70] Y.Y. Wang, Z.H. Ni, Z.X. Shen, H.M. Wang, and Y.H. Wu Interference Enhancement of Raman Signal of Graphene. *Journal of Physical Chemistry*, 122:14865–14871, 2018.

[71] D. Metten, F. Federspie, M. Romeo, and S. Berciaud. All-optical Blister Test of Suspended Graphene using micro-Raman Spectroscopy. *Physical Review Applied*, 2(054008), 2014.

[72] D. Metten, G. Froehlicher, and S. Berciaud. Monitoring Electrostatically-induced Deflection, Strain and Doping in Suspended Graphene using Raman Spectroscopy. *2D Materials*, 4(014004), 2016.

[73] D. Metten. Probing the Opto-Electronic and Mechanical Properties of Suspended Graphene Membranes by Raman Spectroscopy. *Ph.D. Thesis*, 96–99, 2016.

[74] K. S. Kim, Y. J. Ji1, Y. Nam, K. H. Kim1, E. Singh, J. Y. Lee, and G. Y. Yeom. Atomic Layer Etching of Graphene Through Controlled Ion Beam for Graphene-based Electronics. *Scientific Reports*, 7(2462), 2017.

[75] Y. Colombe, T. Steinmetz, G. Dubois, F. Linke, D. Hunger, and J. Reichel. Strong Atom-Field Coupling for Bose-Einstein Condensates in an Optical Cavity in a Chip. *Nature*, 450:272–276, 2007.

[76] A. R. Plantey, S. Klyatskaya, V. Reita, L. Marty, O. Arcizet, M. Ruben, N. Bendiab, and V. Bouchiat. Time- and Space-Modulated Raman Signals in Graphene-based Optical Cavities. *Journal of Optics*, 15(11), 2013.

[77] A. Dash, U. Palanchoke, M. Gely, G. Jourdan, S. Hentz, S.K. Selvaraja, and A.K. Naik. Enhanced All-Optical Cavity-Tuning Using Graphene. *Optics Express*, 7(23), 2019.

[78] Q. Ma, C.H. Liu, J.C.W. Song, Y. Lin, J.F. Kong, Y. Cao, T.H. Dinh, N.L. Nair, W. Fang, K. Watanabe, T. Taniguchi, S.Y. Xu, J. Kong, T. Palacios, N. Geidk, N.M. Gabor, and P. Jarillo-Herrero. Giant Intrinsic Photoresponse in Pristine Graphene. *Nature Nanotech.*, 14:145–150, 2019.

[79] N. Petrone, C. R. Dean, I. Meric, A. M. van der Zande, P. Y. Huang, L. Wang, D. Muller, K. L. Shepard, and J. Hone. Chemical Vapor Deposition-Derived Graphene with Electrical Performance of Exfoliated Graphene. *Nano Letters*, 12:2751–2756, 2011.

[80] M. A. Muriel, and A. Carballar. Internal Field Distributions in Fiber Bragg Gratings. *IEEE Photonics Technology Letters*, 9(7), 1997.

[81] X.D. Zhu, J. P. Landry, Y.S. Sun, J.P. Gregg, K.S. Lam, and X.W. Guo. Oblique-Incidence Reflectivity Difference Microscope for Label-Free High-Throughput Detection of Biochemical Reactions in Microarray Format. *Applied Optics*, 46(10):1890–1895, 2007.

[82] S. Y. Lee, T. Y. Jeong, S. Jung, and K. J. Yee. Refractive Index Dispersion of Hexagonal Boron Nitride in the Visible and Near-Infrared. *Advances in Physics Semiconductors*, 256(6), 2019.

[83] S. Reich, A.C. Ferrari, A. Arenal, A. Loiseau, I. Bello, and J. Robertson. Resonant Raman Scattering in Cubic and Hexagonal Boron Nitride. *Physical Review B*, 71(205201), 2005.

[84] S. Cheon, K. D. Kihm1, H. G. Kim, G. Lim, J. S. Park, and J. S. Lee. How to Reliably Determine the Complex Refractive Index (RI) of Graphene by Using Two Independent Measurement Constraints. *Scientific Reports*, 4(6364), 2015.

[85] B. G. Ghamsari, J. Tosado, M. Yamamoto, M. S. Fuhrer, and S. M. Anlage. Determination of the Optical Index for Few-Layer Graphene by Reflectivity Spectroscopy. *Scientific Reports*, 6(34176), 2016.

[86] G.J. Melin. Spatial Dependence of Photocurrent and Photogeneration Mechanisms in Graphene Field Effect Transistors. *M.Sc. Thesis*, 52–53, 2020.

[87] L. Zhang, Z. Lu, Y. Song, B. Bhatia, K.R. Bagnall, and E.N. Wang. Thermal Expansion Coefficient of Monolayer Molybdenum Disulfide Using Micro-Raman Spectroscopy. *Nano Letters*, 7:4745–4751, 2019.